

Gamma-ray data collection, calibration and analysis for Lorentz invariance violation studies

Jelena Strišković,^a Anna Campoy-Ordaz^b and Julien Bolmont^{c,*}

^a*Josip Juraj Strossmayer University of Osijek, Department of Physics,
Trg Ljudevita Gaja 6, 31000 Osijek, Croatia*

^b*Departament de Física, Universitat Autònoma de Barcelona and CERES-IEEC,
Carretera de Bellaterra a l'Autònoma, 08193 Bellaterra, Spain*

^c*Sorbonne Université, CNRS/IN2P3,
Laboratoire de Physique Nucléaire et de Hautes Energies, LPNHE,
4 Place Jussieu, F-75005 Paris, France*

E-mail: bolmont@in2p3.fr, jstriskovic@fizika.unios.hr, anna.campoy@uab.cat

This manuscript presents the lecture notes of a course given during the second training school of COST Action CA18108 “Quantum gravity phenomenology in the multi-messenger approach”, which occurred in Belgrade in September 2022. It aims to provide a comprehensive introduction on various aspects of data acquisition and analysis in the context of high-energy gamma-ray astrophysics. A special effort was made so that these lecture notes can be understood by PhD students with no background on instrumentation or gamma-ray astrophysics. So that the lecture is kept short enough, the choice was made to focus on the imaging atmospheric Cherenkov technique. These lecture notes will walk the reader through the whole analysis process: how raw images are collected and how the raw data are produced, how these raw data are calibrated, how primary particle parameters are reconstructed and how the physical properties of the observed source are extracted. Finally, we will go through the different important points to consider regarding hardware, reconstruction and analysis when Lorentz Invariance Violation (LIV) studies have to be carried out.

Second Training School of COST Action CA18108 “Quantum gravity phenomenology in the multi-messenger approach”

3-10 September 2022

Belgrade, Serbia

*Speaker

Contents

1	Introduction	3
2	Some basics: signal, background, and other general considerations	5
2.1	Signal and background	5
2.2	Extensive air showers	7
2.3	A first look at the analysis process	11
3	From image collection to raw data	13
3.1	An overview of a camera	13
3.2	Pixels and photo-detectors	14
3.3	Raw data acquisition	17
3.3.1	The camera needs to be fast	17
3.3.2	Signal processing	18
3.3.3	Summary	24
4	Calibration	25
4.1	Overview	25
4.2	Pedestal	25
4.3	Gain calibration	27
4.4	Flat-field	29
4.5	Summary: from ADC counts to a charge in photo electrons	29
4.6	From a charge to Cherenkov light intensity	30
4.7	Summary	32
5	Reconstruction and analysis	32
5.1	Reconstruction	33
5.1.1	Hillas reconstruction	34
5.1.2	Model reconstruction	41
5.1.3	From reconstruction to analysis, and detector performance	44
5.1.4	Summary	47
5.2	Analysis	49
5.2.1	Background estimation	49
5.2.2	Significance	51
5.2.3	Control plots	52
5.2.4	A glimpse on spectrum determination	53
5.2.5	Sensitivity	54
6	Lorentz invariance violation analysis	55

7 Conclusion

57

1. Introduction

Gamma-ray astronomy focuses on the electromagnetic signal produced by distant sources in the Universe, with energies typically above a few hundred kiloelectron-volts (keV). The energy range is usually further split into two parts: the high energy (HE) domain, up to a few hundreds of GeV, and the very-high energy (VHE) domain, above a few tens of GeV, and up to a few hundred TeV. The exact location of the boundary between the two ranges is somewhat arbitrary, and another classification can be adopted: the HE domain is the one where detectors onboard satellites have to be used, while the VHE domain is where detectors on the ground are the best option. There are several reasons for that:

- The gamma-ray flux is higher at lower energies, and decreases as a power-law of the energy, meaning that small collection areas are possible in the HE regime, but certainly not in the VHE regime.
- Primary gamma rays with energies below ~ 10 GeV do not usually give any useful signal for ground-based detectors unless they are located at impractically high altitudes.
- At energies above a few hundred GeV, detectors in space are typically too small to allow a full energy deposit of the primary gamma, and therefore suffer from bad reconstruction performance.
- The size and weight of detectors in space are limited by the size and performance of the rocket used for the launch. The typical collection area of a gamma-ray telescope satellite like *Fermi* is of the order of 1 m^2 .
- The size of arrays of ground-based detectors, or the number of detectors is usually only limited by cost constraints. Still, the collection area reaches a cumulative value of the order of 1000 m^2 with present-day instruments.

Even if their goals are the same, space and ground-based detectors are very different in nature. The main reason for that is the fact the atmosphere is opaque to gamma rays. VHE photons interact in the atmosphere, producing an electromagnetic (EM) shower, that is a cascade of secondary particles, photons, electrons and positrons. The primary photon disappears, but electrons and positrons of the shower produce Cherenkov radiation, which can reach the ground. On the contrary, space-based detectors detect the primary photons directly through the photo-electric effect, Compton scattering, or pair production. If we skip the problem of data-reduction and transmission to the ground which is specific to space-based instruments, there is no fundamental difference between a detector in space, and a detector designed for experiments at colliders such as the LHC. Taking *Fermi* Large Area Telescope (LAT) as an example, a Silicon tracker is used to convert photons and measure the e^\pm tracks, and a calorimeter measures the energies of electrons and positrons. For that reason, and

because a lot of material can be found about detection techniques at play at colliders, we will focus on ground-based gamma-ray detectors operating in the VHE range, so from a few tens of GeV to a few hundreds of TeV.

The essential feature of ground-based gamma-ray detectors is the fact they use the Earth's atmosphere as the primary photon interaction medium. VHE photons produce cascades of secondary particles in the atmosphere. These particles (mainly electrons and positrons) emit Cherenkov light and this light is collected by telescopes. These are called Imaging Atmospheric Cherenkov Telescopes (IACTs) because the camera in the focal plane of the telescope makes an image of the shower through its Cherenkov light emission. A crucial point is that atmosphere is an ever-changing, complex medium. It obviously shows gradients in pressure and temperature with respect to altitude. Also, atmosphere aerosol content is a key factor that has a direct impact on detection performance. Transparency is indeed very important since the more Cherenkov light is absorbed, the less signal reaches the cameras. Therefore, proper modelling of the atmosphere and dedicated monitoring of its transparency are critical for the reliability of ground-based gamma-ray astronomy.

Even before going into the details of the Cherenkov technique, it is necessary to say a few words about the physical object that we actually detect: atmospheric showers. Also, even if we are interested in photons produced by distant pulsars, blazar jets or other more exotic phenomena like dark matter annihilation, there is an even higher number of protons hitting the atmosphere. These protons form a background. All these basics will be covered in §2.

The basic output provided by an IACT is the raw image of the Cherenkov light emitted by an atmospheric cascade, namely an array with each cell representing a pixel of the camera, filled with numerical values. Section §3 will deal with how the image is made, i.e. how the raw data is collected from the Cherenkov photons hitting the camera.

Then, it is essential to relate raw data to some physical quantities, namely the charge collected, and the corresponding Cherenkov light intensity. This is the goal of the calibration step, which will be described in §4.

Finally, we will explore reconstruction and analysis steps in §5. Reconstruction is the level where shower images are processed to discriminate gamma-like and hadron-like events and to reconstruct shower parameters such as energy or direction. The analysis consists in extracting astrophysical source characteristics (energy spectrum, light curve) from a large number of reconstructed events. Importantly, it is also at the analysis level that the statistical significance of an observation can be assessed.

Since this lecture was given at a training school organized by the COST Action CA18108 “Quantum gravity phenomenology in the multi-messenger approach”, and as the title suggests, we could not completely ignore the topic of how spectrum and light curve are further processed to extract constraints on Lorentz Invariance Violation (LIV). This will be addressed in §6. We will give some concluding remarks in §7.

Before going into the details, please note that because the lecturer is part of the H.E.S.S.¹ (High Energy Stereoscopic System) collaboration, these notes will mostly (but not only) focus on how H.E.S.S. works and how data are analyzed in this particular experiment. Other IACTs operate on the same principles, but there may be slight differences in terminology or vocabulary. However, the

¹<https://www.mpi-hd.mpg.de/hfm/HESS/>

knowledge gained from these notes will allow the reader to fully comprehend experimental articles written by any IACT collaboration. Four major IACT experiments are currently in operation. In addition to H.E.S.S., located in Namibia, there are VERITAS² operating in the Arizona desert in the United States, and MAGIC³ and LST-1⁴ in the Canary Islands (La Palma). LST-1 (Large-sized telescope 1) is a prototype, part of the future Cherenkov Telescope Array (CTA), currently in the commissioning phase and already producing scientific publications.

Finally, it is worth noting that some advanced technical details have been ignored in these notes.

2. Some basics: signal, background, and other general considerations

2.1 Signal and background

Gamma-ray astronomy obviously focuses on photons, which constitute the *signal*. Unfortunately, the flux of photons is usually very small as compared to that of protons, which constitute the main *background*, the so-called *hadronic background*.

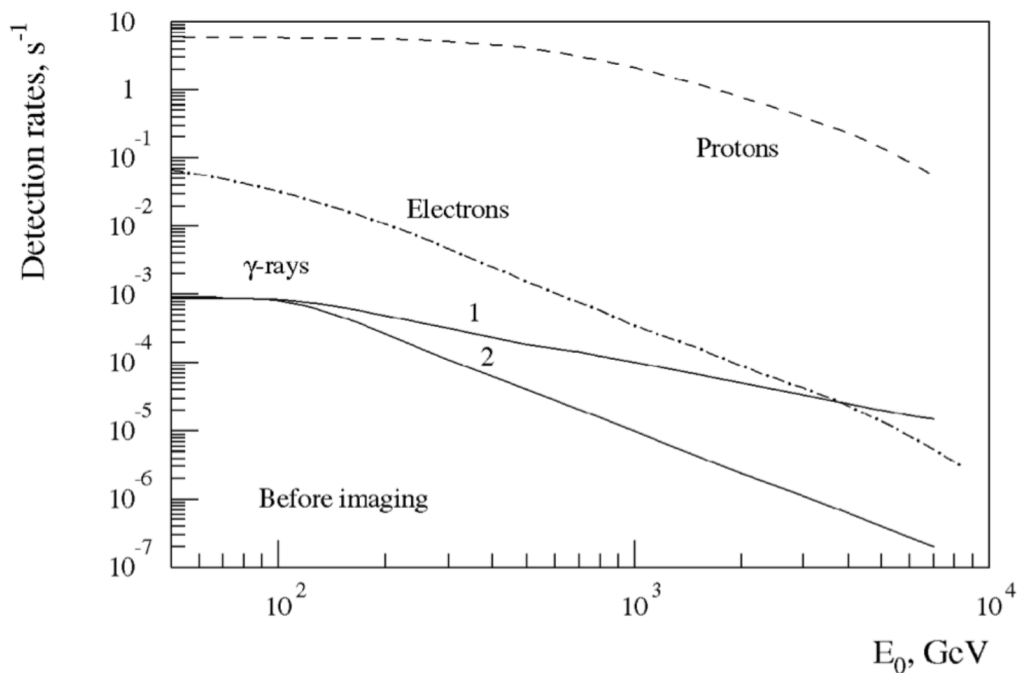


Figure 1: Typical gamma ray, proton and electron spectra. Gamma-ray spectra labelled 1 and 2 correspond to spectral indices of $\alpha = 2$ and 3 , respectively. Figure from [1].

Figure 1 shows the difference in flux between gamma rays, protons and electrons. In the VHE range, spectra (flux vs energy) usually show a decrease following a power law E^α , where the exponent α is called the *spectral index*. Two values for the spectral index are shown in the figure,

²<https://veritas.sao.arizona.edu>

³<https://magic.mpp.mpg.de>

⁴<https://www.lst1.iac.es>

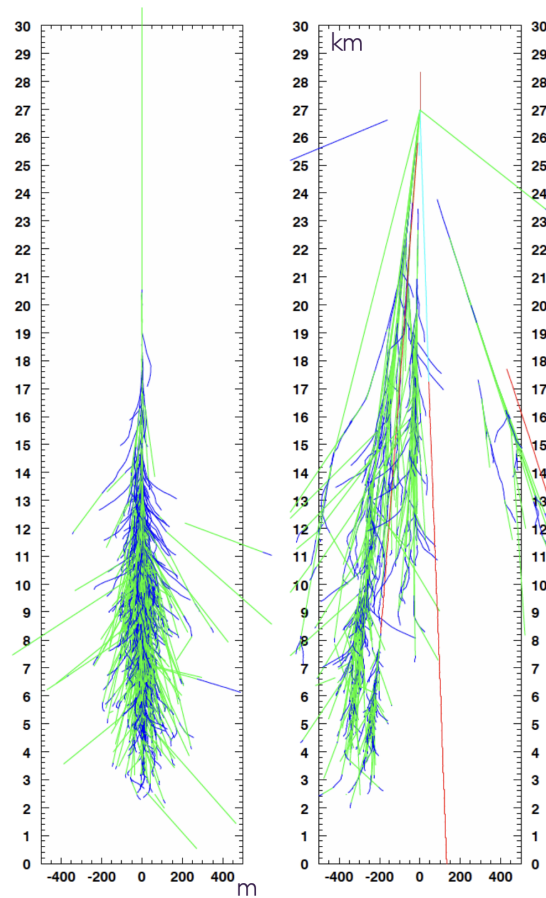


Figure 2: Simulated atmospheric showers. A 300 GeV photon (left). A 300 GeV proton (right). Note the scales are different in the vertical and horizontal directions. Green tracks correspond to photons; blue tracks are electrons or positrons. All other particle types are shown in red. Figure from [2].

resulting in different slopes in a log-log representation. Proton flux is far above the gamma-ray flux, while electrons stand in between. It is then necessary to discriminate between particles and isolate gamma rays by rejecting as many background particles, protons and electrons, as possible. In other words, we need high *rejection factors*, typically of the order of 100 to 10000, depending on the slope of the gamma-ray spectrum, and on the energy range considered. This means that we need to reduce the hadronic background by a factor of 100 to 10000. We will see later how it is done using *discrimination variables* (§5). Rejection of the proton background is primarily done taking advantage of the fact hadronic showers have different shapes (or geometries) than electromagnetic cascades (more on that later in this section). But for electrons, which also produce electromagnetic showers, this feature cannot be used. For both electron and proton backgrounds, an additional characteristic feature has to be used: they are both isotropic in the sky, or at least in the part of the sky which falls into the field of view of IACT cameras. Going a step further, it has to be mentioned that there is also a *gamma-ray background*, due to unresolved galactic or extragalactic sources. In this case, only the angular distribution can be of any help to discriminate between signal and background photons.

2.2 Extensive air showers

IACTs detect nanosecond flashes of Cherenkov light produced by extensive air showers (EAS) initiated when a very high energy gamma ray or cosmic ray enters Earth's atmosphere and interacts with the nuclei in its upper layers. Photons and hadrons produce electromagnetic and hadronic showers, respectively. Figure 2 shows a typical electromagnetic shower generated by a 300 GeV photon (left), and a hadronic shower resulting from a proton interaction with the same energy (right). First, we can point out that the altitude scale is in kilometers while the horizontal scale is in meters. Hence, showers are very narrow and very long. Also, a clear difference can be noticed between the two types of showers. This difference comes from the fundamental processes involved as the shower develops. In the case of the electromagnetic shower, Bremsstrahlung and pair creation are at play, especially in the initial stages of shower development. As the shower propagates, the energy of the secondary particles decreases and photons will start interacting through Compton scattering and ultimately through photoelectric absorption. On the other hand, a hadronic shower involves the creation of numerous heavy particles with nuclei fragments, muons, pions and neutrinos. Among these, π^0 particles lead to the formation of secondary, electromagnetic-type sub-showers. It can happen that for some hadronic showers, the π^0 contribution dominates the Cherenkov light output. In these cases, it can be a challenge to distinguish between hadronic and electromagnetic showers.

Figure 3 shows several realisations of simulated electromagnetic (top) and hadronic showers (bottom). It can be noticed that while electromagnetic showers exhibit relatively uniform sizes and shapes across different instances, hadronic showers display considerable variation from one instance to another. In both Figure 2 and Figure 3, photons are represented by green tracks, while electrons or positrons are shown in blue. All remaining particles, including muons, are depicted in red. Notably, relativistic muons are the dominant type of particles produced in hadronic interactions which are able to reach the ground.

As the charged particles, such as electrons, positrons or muons, travel through a dielectric medium with a speed greater than the speed of light in that medium, the polarisation of the medium becomes asymmetrical along the particle's path. As these particles move, the molecules of the medium return to their ground state, releasing photons in the process, which is known as Cherenkov radiation. The mirrors of each IACT telescope collect this Cherenkov light and reflect it onto their respective cameras where they are collected. Figure 4 shows other simulated electromagnetic and hadronic showers, but this time the two plots at the bottom show the pattern of Cherenkov light as it reaches the ground. The distinctive ring-shaped distribution of Cherenkov photons on the ground is characteristic of an electromagnetic shower (bottom left). For hadrons, we can observe dense clusters due to muons and thin rings due to the faint electromagnetic components. Cherenkov photons emitted by muons, when collected by the telescope and focused onto the camera, will result in characteristic rings on the camera plane.

Figure 5 shows the direction of Cherenkov light emission at different altitudes as dashed lines. As the shower progresses, the charged particles, which emit Cherenkov photons, lose energy and their speed decrease consequently. This leads to an increase, or "opening", of the Cherenkov emission angle. When compounded with the fact that there are significantly more particles at a 10 km altitude (the "*shower maximum*") as compared to the shower's endpoint, the result is the characteristic Cherenkov ring distribution observed on the ground (Figure 4).

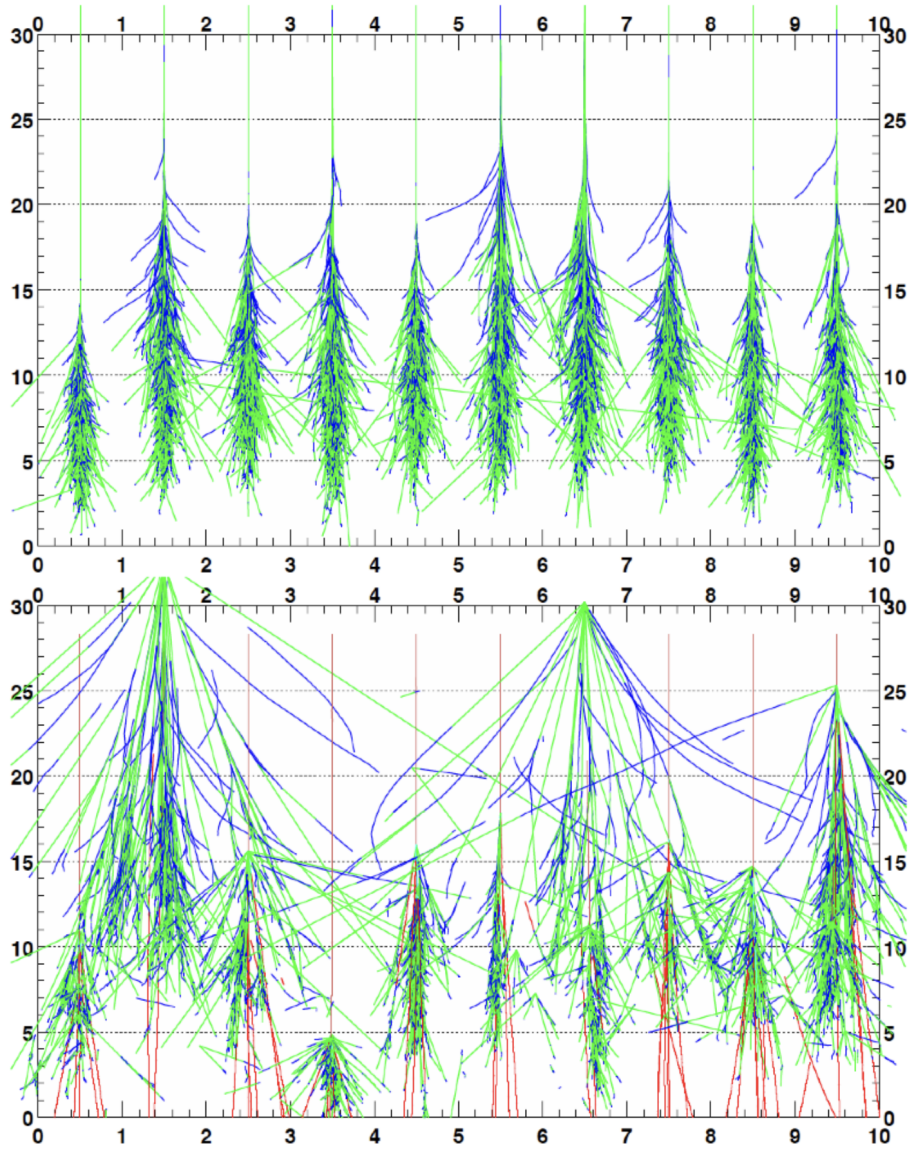


Figure 3: Several realisations of the atmospheric shower. 300 GeV photons (top). 300 GeV hadrons (bottom). Green tracks correspond to photons; blue tracks to electrons or positrons. The tracks for all the other types of particles are depicted in red. The altitude is given in kilometers, while the X axis scale is only used to number the different simulations. Figure from [2].

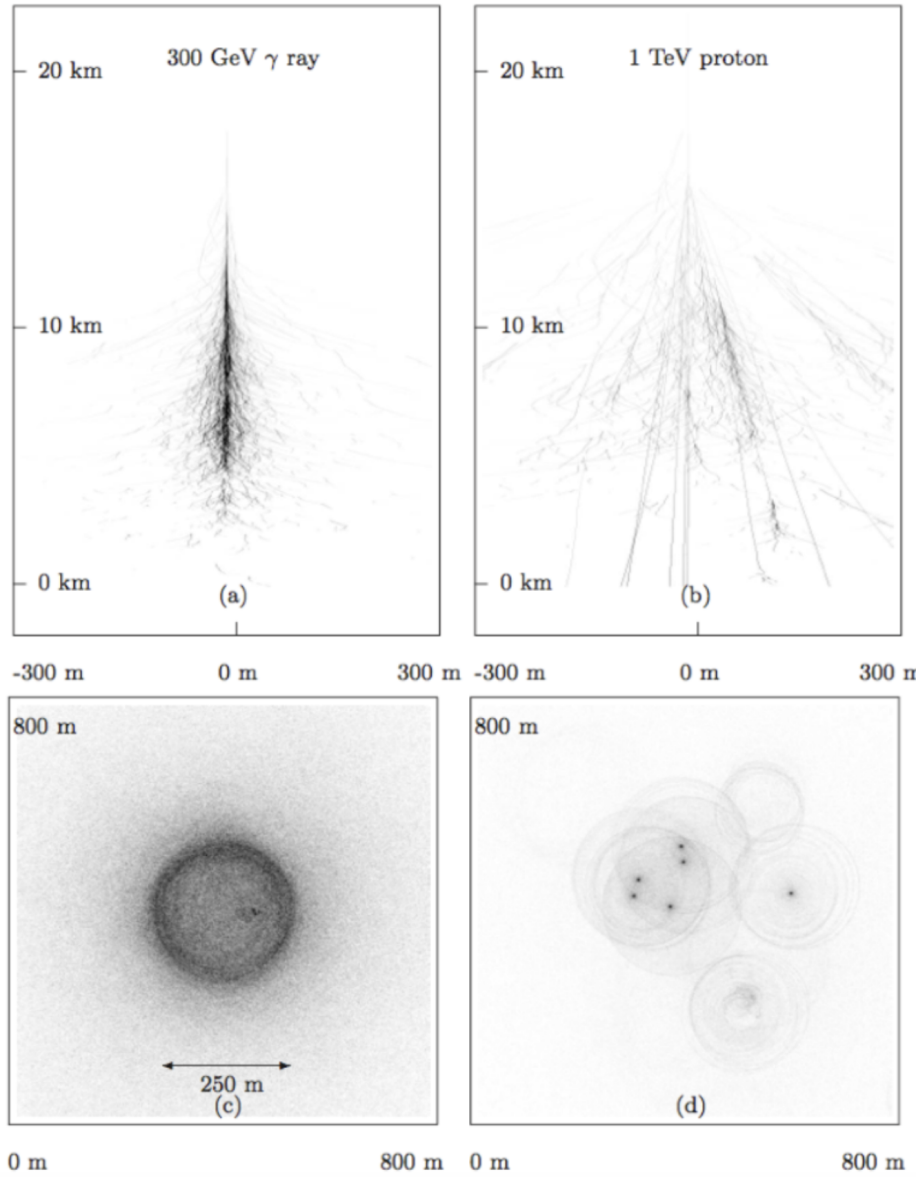


Figure 4: Other simulated showers, this time showing the Cherenkov light distribution on the ground (bottom). A 300 GeV photon (left). A 1 TeV hadron (right). Note the differences of the Cherenkov light pool patterns for a photon and a hadron. Courtesy of S. Funk.

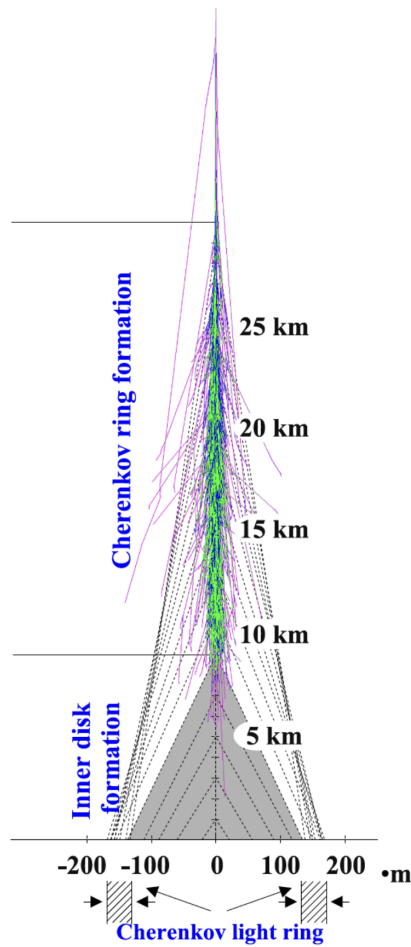


Figure 5: Yet another depiction of an atmospheric shower, this time showing the trajectories of a few Cherenkov photons as dashed lines. Note that the horizontal plane is in meters while the vertical scale is in kilometers. Figure from [3].

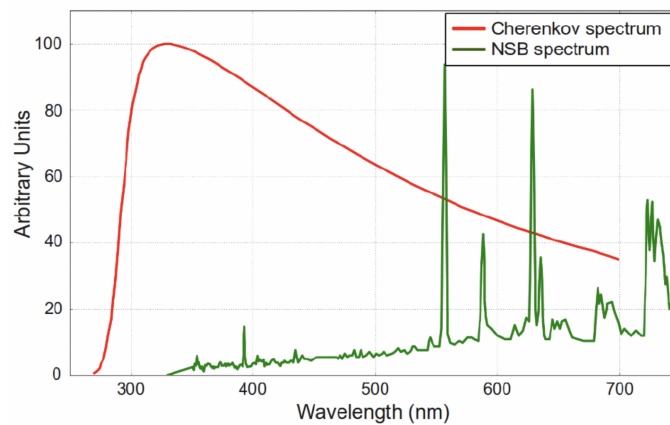


Figure 6: The spectrum of Cherenkov light emission (in red), peaking around 320 nm. The NSB spectrum is shown in green. Figure from [4].

IACTs are optical telescopes designed specifically to collect Cherenkov light. However, an inherent challenge is that the mirrors reflect all other types of light, collectively known as the Night Sky Background (NSB). The NSB includes light emitted by stars (including stars in the Milky Way), as well as other types of light pollution. As an example, the Sun and the Moon, even when they are below the horizon but close enough to it can contribute to the NSB because their light can be scattered in the aerosols of the atmosphere. Figure 6 shows the spectrum of Cherenkov emission (in red), which peaks around 320 nm and the spectrum of the NSB (in green). Ideally, we strive to eliminate NSB as much as possible, and various techniques are available to accomplish this. As the Cherenkov emission is faint, we must employ highly sensitive photodetectors. The photodetectors we will be discussing, and which are widely used for these types of experiments, are Photomultiplier Tubes (PMT). These devices can detect a single photon generating a measurable electrical signal in response. Due to their high sensitivity, PMTs cannot operate under high luminosity. Therefore, IACTs only observe at night and, more specifically, on nights with minimal moonlight. The moon's reflection of sunlight on Earth is so intense that it could potentially damage the PMTs.

To close this section, let us point out that the time a 1 TeV cascade takes to develop is of the order of ~ 10 ns. This is also the duration of Cherenkov light emission. This is critical information to take into account for the design of the camera.

2.3 A first look at the analysis process

The development of the shower and the emission of Cherenkov radiation occur within ~ 10 ns. Due to the faint and short-lived nature of the Cherenkov light signal, large mirrors and fast, sensitive cameras are required for IACTs. The fact Cherenkov emission is faint requires large collection areas and sensitive photo-sensors. For example, the primary mirror of the large telescope in H.E.S.S. spans 600 m^2 , while smaller ones are approximately 100 m^2 . Also, the camera and electronics must be capable of capturing images in roughly ten nanoseconds. Consequently, the camera and electronic systems must exhibit sufficient speed to capture these fleeting events accurately.

The particle detection process involves not only identifying the particle type, such as distinguishing between a gamma-ray or a hadron but also a comprehensive characterisation of particle's properties. This characterisation entails discerning the primary energy, direction, impact location, and the specific time when the particle is detected. One might consider the timing information as a consequential byproduct, as it is typically provided by the detection apparatus itself. For instance, all our detectors are equipped with Global Positioning System (GPS) clocks, which are utilised to timestamp every detected particle with a sub-microsecond precision.

An important concept in experimental (astro-)particle physics is the idea of *event*. In the context of IACTs, an event is the interaction of a gamma-ray or a hadron with the atmosphere. This interaction creates Cherenkov light, which is then reflected by a mirror and captured by a camera. Since the mirror and the camera do not receive only Cherenkov light from atmospheric showers, but also light from stars and other light-emitting objects (the NSB mentioned in the previous section), we obviously do not want to record data all the time. The system used to decide when to collect data is called *trigger*. An event does not technically occur without the camera being triggered, since in that case no data is recorded. Therefore, when referring to an *event*, it is implied that the event has successfully triggered the detector.

The initial type of data we obtain is commonly referred to as *raw data*, which essentially represents the unprocessed output from the detector. This raw data primarily consists of the charge received from each pixel (or each channel) in the camera. The amplified and integrated current pulses are subsequently converted into Analog-to-Digital Converter (ADC) counts. This digital representation, a binary number, is then encapsulated into data blocks and transmitted to a computer farm for further processing. However, raw data cannot be used directly for analysis. To derive meaningful information from the data, a *calibration* process is required. This procedure essentially converts the ADC counts, which are numerical values employed for computer comprehension, into an actual charge expressed in photo-electrons. Calibration also allows the evaluation of optical efficiency, which is necessary to relate ADC counts to Cherenkov photon flux. The charge, in photo-electrons, is then utilised in the subsequent stage known as *reconstruction*. The primary aim of the reconstruction phase is to discriminate between photons and hadrons. Our interest predominantly lies in photons, and our ideal outcome is to retain only these particles while rejecting all others. In practice, this is never possible: even striving to develop the most effective reconstruction software and devise the most discerning discrimination variables, it is important to understand that these tools will never achieve 100% efficiency or reliability. For instance, a proton-induced shower at low energies can resemble an electromagnetic shower to such an extent that it becomes exceedingly difficult to differentiate it from a gamma-ray. As a result, the set of events we look for, gamma events, is contaminated by some hadrons erroneously reconstructed as photons. This is the reason why we use the adjective “*gamma-like*”, indicating a sample that does not consist entirely of photons.

To further try to separate between real gamma events and gamma-like events, the *reconstruction* stage yields relevant parameters that aid to separate photons and hadrons contributions. These so-called *discrimination variables* are numerical values that can be interpreted as probabilities that an event is a real gamma event or a real hadron event. These variables are usually constructed so that the closer to zero the value is, the higher the probability the gamma-like event is a real gamma. Applying more and more stringent *selection cuts* on the discrimination variables gives a sample of gamma events with a higher and higher purity, but with less and less statistics. The second goal of reconstruction is to characterise the parameters of the incoming particles, which include primary energy and direction. There are multiple methods to accomplish this, but we will only concentrate on the Hillas [5] and Model [6] methods. While the Hillas method is used by all present-day experiments, the Model⁵ analysis was more specifically designed within the H.E.S.S. collaboration and is heavily used by that experiment.

Following the reconstruction phase, we are left with a list of gamma-like events accompanied by some parameters. The subsequent process of interpreting and examining these results is what we refer to as “*analysis*”. The analysis is applied to gamma-like events for:

- Precise background estimation and subtraction.
- Evaluation of statistical significance. This process requires a good estimation of statistic and systematic uncertainties. Usually, we consider that the source is detected if the significance is equal to or above 5σ .

⁵While the Hillas method is named after its inventor, it is not the case for the Model method. The capital ‘M’ is kept anyway, as in [6].

- For sources which show a significance high enough, the last step will consist in extracting source properties: energy spectrum, light curve and morphology.

We can already stress here that in the end, only if we have a light curve, only if we have a spectrum, only if the light curve shows a significant amount of variability, and only then we will be able to perform a Lorentz invariance violation (LIV) analysis... In addition, knowing the distance of the source, or its redshift for extragalactic objects, is also required. All these conditions explain why only a few sources detected by IACTs have been used so far for these analyses.

3. From image collection to raw data

This section will describe in detail the crucial subsystems that are necessary to convert the image of the cascade Cherenkov emission to what we call *raw data*. This operation is done by the *camera*.

3.1 An overview of a camera

In the context of IACTs, a camera is a device which takes a picture of an atmospheric shower through its Cherenkov emission. The camera is located near the focal plane of a converging mirror, and parallel to it, so that the image of a shower located at an altitude of ~ 10 km is in focus. The picture is made of a number of pixels, each pixel containing information about the intensity of the light received.

Several different architectures have been used to design the IACT camera and its electronics, with different philosophies. As an example, H.E.S.S. cameras [7] are designed so that everything from light collection to raw data generation is done in the camera itself. Also, a large part of the processing (amplification, triggering) is done on analog signals before digitization and encapsulation. Another example is given by the cameras of MAGIC [8], for which only light collection and a first amplification is done at the focal plane. Then, analog signals are converted to optical signals to be sent to a counting house near the telescope through optical fibers. All the other functionalities of the camera (trigger, digitization, etc.) are implemented on the ground. This method allows reducing considerably the weight of the cameras, which in turn allows using light mechanical structures for the telescope, which makes fast movements possible. A last example is the FlashCam [9] which is a fully digital camera, meaning that signal from photo-detectors are amplified and digitized immediately, all the rest of the processing being done on digital signals.

Despite the variety of architectures adopted for camera design, the basic principles are roughly the same. Cherenkov's light falling on the camera is converted into an electrical signal, which is amplified and digitized. Digitization is usually the most time-consuming step, so we do not want to digitize all signals if they are not relevant for science data analyses. Therefore, a trigger system is used to keep as many cascades as possible, while rejecting as much NSB as possible.

In the following, we will base most of our description on the pre-upgrade CT5 camera [10] of the H.E.S.S. array (Figure 7), which operated on the big telescope in the middle of the array (~ 600 m² area mirror, and a focal length of ~ 30 m) between 2012 and 2019.

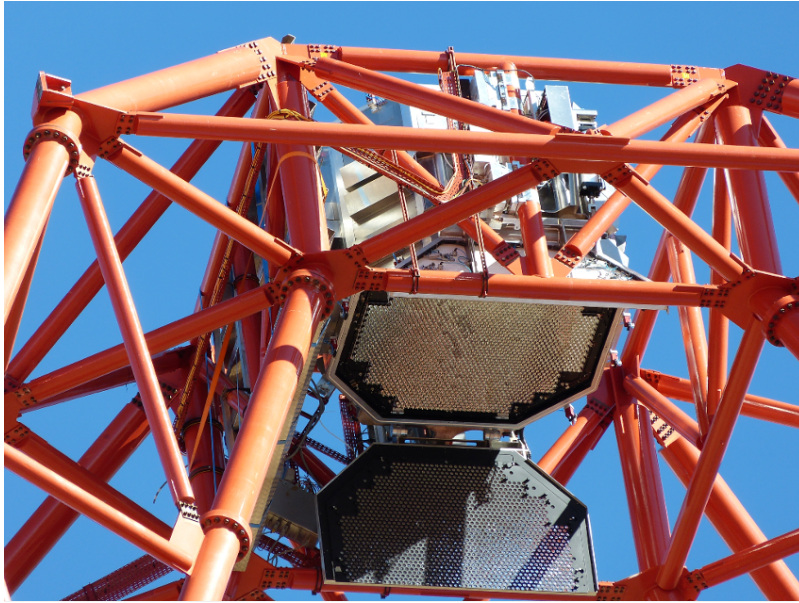


Figure 7: The camera of H.E.S.S. telescope CT5. On this picture, the camera protecting lid is opened so that the pixels can be seen. The camera dimensions are $2.40 \times 2.27 \times 1.84 \text{ m}^3$ with a Field of View (FoV, the part of the sky the camera can see) of 3.2° . It weighs about 2 tons. Credit: H.E.S.S. Collaboration.

3.2 Pixels and photo-detectors

The goal of the camera is to produce an image, and since the assembly of photo-detector responses will be used to make up this image, it is appropriate that each photo-detector is called a “*pixel*”.

In front of each pixel, an optical element called a “*Winston cone*” is usually used to narrow down the field of view, thus reducing the amount of parasitic light reaching the photo-detectors [11].

Up to a recent time and the dawn of new technologies (in particular Silicon photo multipliers [12, 13]), the most commonly used photo-detectors for IACT cameras have been Photo-Multiplier Tubes (PMT). They have been used since the beginning of Cherenkov telescopes, and they will equip CTA cameras. As we will see later in §4, a precise knowledge of PMT characteristics is required in order to properly calibrate raw data. We will then spend the next few paragraphs describing how a PMT works. We will not go too far into the details though, but interested readers will find more details e.g. in [14].

A PMT (Figure 8) is made of glass in which a high vacuum is made so that to minimize electron interactions with residual gas. The entrance window is called *photocathode*. Its goal is to convert photons (in our case Cherenkov photons) into electrons through photoelectric absorption. Due to their production mechanism, these electrons are usually called “*photo-electrons*” or just “*p.e.*”. Due to the stochastic nature of photon interaction, not all photons will be converted into photo-electrons. The probability of a photon being converted into an electron is called *quantum efficiency* (QE). QE is a very important parameter of a PMT, which needs to be measured or at least estimated for an accurate data calibration. The best PMTs available at this time can reach a QE of $\sim 40\%$, but most PMTs used for IACTs have a lower QE of $\sim 30\%$.

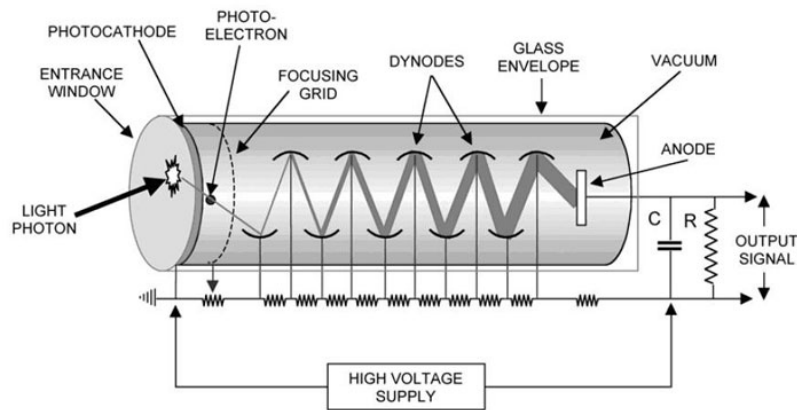


Figure 8: Basic schematics of a PMT showing the different elements discussed in the text. In the context of this lecture, the “light photon” is a Cherenkov photon produced by an atmospheric shower. The figure shows the resistive divider used to provide a different voltage to each dynode so that electrons are always attracted from one dynode to the next while gaining kinetic energy at the same time. Figure from <https://www.sense-pro.org/111-sensors/pmt>.

Photo electrons are then directed to a series of *dynodes*. For this, focusing electrodes are used to generate an electric field so that photo-electrons will reach the first dynode. The probability that a photo-electron reaches the first dynode is called *collection efficiency* (CE). There is no particular technical issues when designing the focusing electrodes so CE is usually very close to 100%.

A dynode is an electrode which is coated with a material with a good secondary electron emission. A series of dynodes is used to multiply the number of electrons. Each dynode is polarized to a different voltage so that electrons are guided and accelerated from one dynode to the next. The kinetic energy of each electron impinging on a dynode is converted to produce several secondary electrons. The overall multiplication factor obtained with all the dynodes (typically 8 or 10) is called the *gain* of the PMT. For IACT cameras, the gain is typically tuned to be of the order of 10^5 , meaning a single p.e. produced at the photo-cathode and collected by the first dynode will give 10^5 electrons. It is important to note that it is possible to set the gain as desired. For this, the voltage used to polarize the dynodes can be adjusted. For example, the PMTs of the H.E.S.S. camera of CT5 can be set to a gain of 2×10^5 with a voltage of ~ 800 V, spread out over the dynodes using a voltage divider. Note however that the voltage necessary to achieve a particular gain is different from one PMT to another. As we will see later, calibration is used to set the correct high voltage to each PMT so that all of them have the same gain. Gain discrepancies are taken into account in data analysis.

Electrons moving in the tube need to be protected from external magnetic fields. For that reason, PMTs are encapsulated in a mu-metal⁶ casing.

In the end, all the secondary electrons produced by the dynodes are collected by a last electrode, the *anode*, where they produce a current pulse (Figure 9). Overall, the time spent between a photon hits the photocathode and the corresponding current pulse produced at the anode is a few tens of

⁶Nickel–iron soft ferromagnetic alloy with very high permeability, <https://en.wikipedia.org/wiki/Mu-metal>.

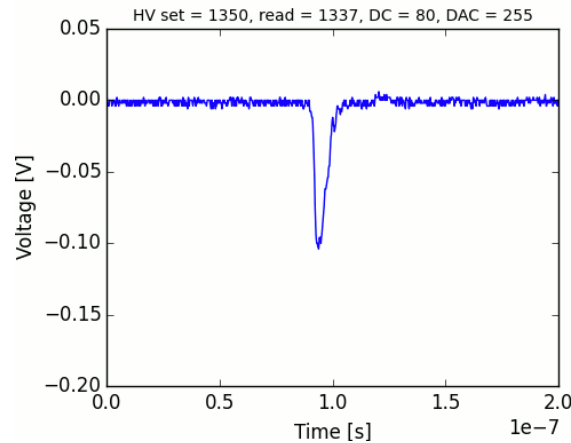


Figure 9: Example of the pulse collected at the anode of a H.E.S.S. PMT. Even though a current pulse is produced, this current pulse translates into a voltage pulse due to the resistive circuit connected to the anode. The integration of this pulse gives the charge collected at the anode. Credit: H.E.S.S. Collaboration.

nanoseconds. The width of the current pulse is close to 3 ns for CT5 PMTs.

It is important to note that PMTs are always used in a regime where there is a *linear relation* between the amount of light collected at the cathode and the current pulse amplitude and integral (electric charge) at the anode.

As mentioned earlier, PMTs can only work because all their internal elements are in vacuum. This vacuum is required because the electrons need to propagate from one dynode to the next without interacting and being lost on their way. However, whatever efforts are put into manufacturing quality, there is always a small quantity of residual gas in the tube. When a molecule of that gas is hit by electrons from the main signal pulse (the one caused by a photon hitting the cathode), an ion can be produced (mainly H_2^+ , He^+ , CH_4^+). This ion, since it has a positive charge, moves backwards at a much lower speed than electrons, until it hits a dynode or another element of the tube. This impact produces secondary electrons which can propagate to a dynode and then from this dynode to the next and produce a signal at the anode. This signal is called “*afterpulse*” because it is delayed typically by 0.3 to 1 μs as compared to the main pulse. We will see later how afterpulses affect the setting of the trigger threshold.

We conclude that section by giving some more numbers concerning the CT5 camera. The camera consists of 2048 PMTs so the resulting image has 2048 pixels. PMTs are grouped in 128 clusters of PMT, called “*drawers*”, each formed by 16 PMT sharing the same mechanical structure (see Figure 10). We will describe the drawers and how they work in more depth later. Using clusters of PMT helps with maintenance operations. Drawers are mounted into the camera so that they can easily be removed and replaced in case of a malfunction. Each PMT has a diameter of 29 mm and is most sensitive in the wavelength range between 270 and 650 nm, with a peak sensitivity of around 420 nm. As can be seen from Figure 6, the PMT is chosen so that its maximum sensitivity matches the maximum Cherenkov emission as closely as possible.

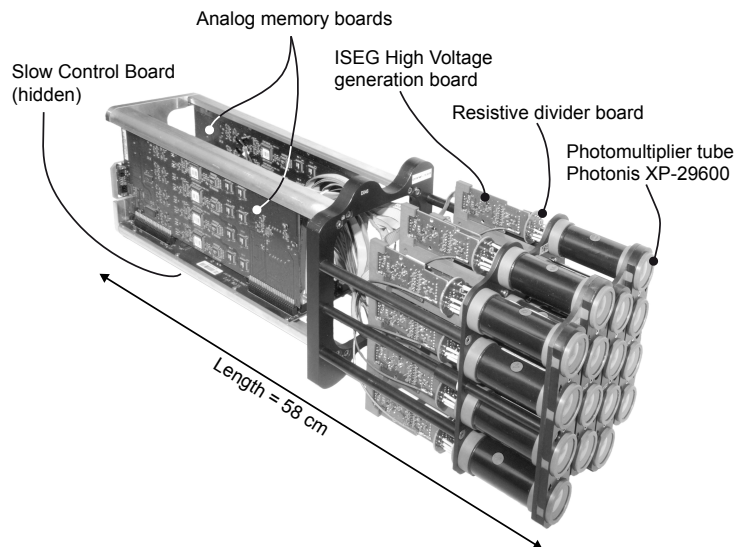


Figure 10: The basic block of CT5 camera front-end electronics, called “*drawer*”. Figure from [10].

3.3 Raw data acquisition

As already briefly discussed in §2.3, raw data is basically a charge expressed in p.e., computed from the amplified anode signal, and converted into a digital number, for each pixel. In section §3.3.2, we will look at these different steps, but before that, we need to discuss a key point for the design of camera electronics.

3.3.1 The camera needs to be fast

It is common sense in the design of any data acquisition system that the characteristics of the system need to match the ones of the *signal of interest*. In our case, the signal we are looking at, an atmospheric shower, is very short with a duration of around 10 ns. In addition, as explained in §2, two types of light signals are received by the camera: the *flash* of Cherenkov light emitted by an atmospheric shower, and a *continuous* light signal due to the NSB. This information is essential when deciding what is the best time window to record a picture (corresponding to the exposure time of any consumer camera).

Figure 11 shows several simulated pictures as taken by a Cherenkov telescope camera, with different exposure times, and taking into account both NSB and the Cherenkov signal. For long exposure time, the light signal collected is uniformly distributed on the camera⁷. It is dominated by the NSB. When the exposure time is smaller and smaller, less continuous signal from the NSB is accumulated, and the transient event due to the cascade can emerge more and more.

As a summary, the camera needs to record a Cherenkov light signal which is ~ 10 ns long. Considering that this Cherenkov signal translates into PMT pulses which have a duration of a few nanoseconds, it is clear why electronics need to be *fast*, meaning it has to deal with fast (and short) signals. Therefore, it is no surprise that Cherenkov technique benefited a lot from the development of GHz electronics.

⁷Note however that bright stars would appear as hotspots in the picture.

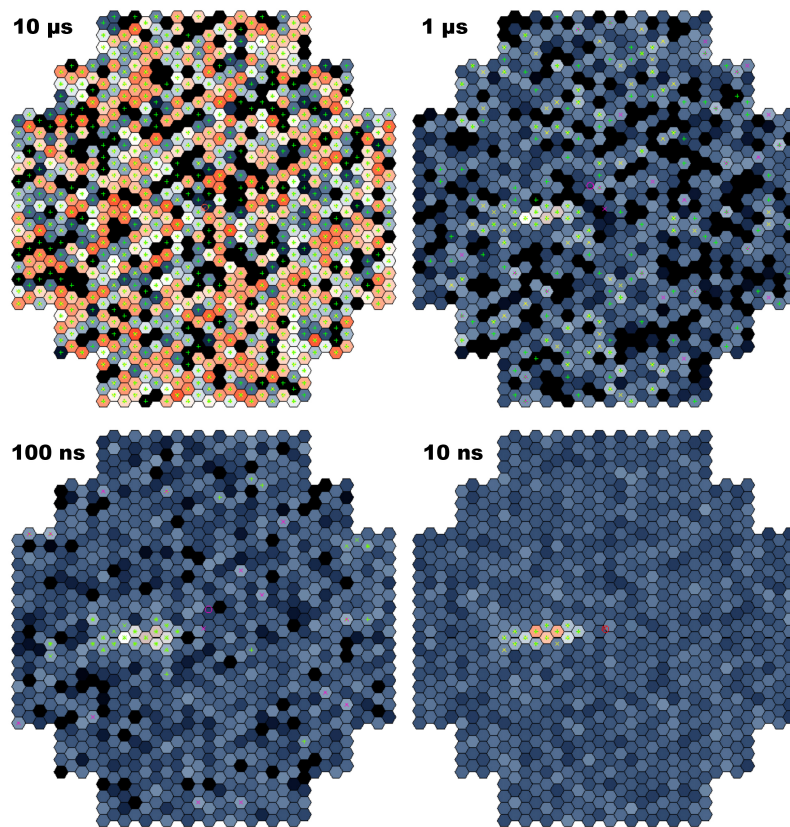


Figure 11: Images obtained by a Cherenkov telescope camera, using different exposure times (simulations). From top to bottom and left to right, the exposure time is $10\ \mu\text{s}$, $1\ \mu\text{s}$, $100\ \text{ns}$, and $10\ \text{ns}$. For $10\ \mu\text{s}$, the NSB dominates, resulting in a random pattern on the camera while for $10\ \text{ns}$, the cascade can clearly be seen. Courtesy of S. Ohm.

3.3.2 Signal processing

Figure 12 shows a simplified view of the H.E.S.S. front-end electronics as designed for the CT5 camera, corresponding to the drawer shown in Figure 10. PMTs are on the left. Each one of them is connected to a circuit which is used to generate and monitor the high voltage (“Active base”). Anode signals are sent to two “Analog Memory Boards”, each one dealing with 8 PMTs (16 PMTs in total). Anode signals are amplified before being sent to the trigger (“Trigger channel”) or to analog memories. When a trigger is received, analog memories are readout and the charge is converted to a digital value by an ADC before being encapsulated in raw data blocks and sent to a computing farm for further processing. The “Slow Control Board” is used to monitor various working parameters such as PMT high voltage and drawer temperatures.

The various elements mentioned are discussed in the following paragraphs.

Amplifiers The pulses obtained from a PMT have an amplitude which is proportional to the amount of light received. Except for very energetic showers, which produce a lot of Cherenkov photons, the signal amplitude is usually low ($\sim 100\ \text{mV}$). It is necessary to amplify it before any further processing. Low-noise, carefully chosen amplifiers are used so that to keep signal-to-noise

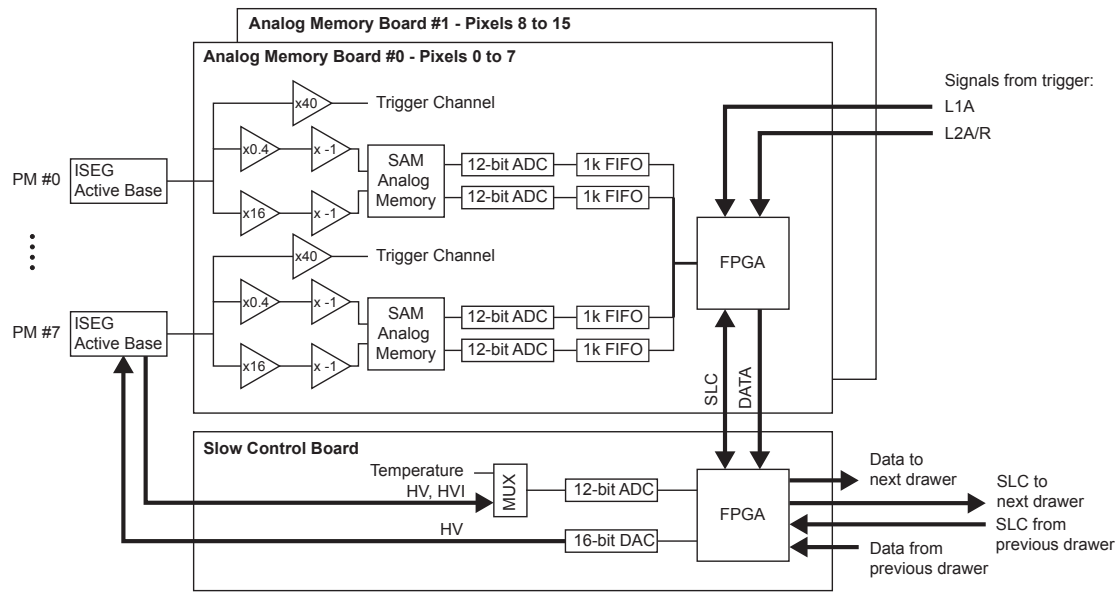


Figure 12: Simplified schematic of a H.E.S.S. CT5 camera drawer showing the main elements of the signal processing chain. Amplifiers are represented with triangles with the value of the gains. See the text for details. Figure from [10].

ratio as high as possible. They also need to be linear on a wide range of input signal amplitude.

In the H.E.S.S. CT5 camera, linear amplifiers are used with three different gains. For low amplitude signals, corresponding to a small collected charge < 200 p.e., a high gain (noted HG, $\times 16$) amplification is applied to the signal. In that channel, a charge of 1 p.e. corresponds to a ~ 7 mV amplitude for the amplified signal. For high amplitude signals, with a collected charge < 5000 p.e., a low gain (LG, $\times 0.4$) amplification is applied to the signal so that electronics does not saturate. In addition, a very high gain $\times 40$ is applied to generate a signal for the trigger (see below). Since only the rising edge of this signal is important, saturation is not an issue.

Figure 13 shows the linearity relation between intensity and the measured charge of the high and low gain channels for H.E.S.S. small telescope post-upgrade cameras. The low-gain amplifier is affected by intrinsic electronic noise at low amplitudes (below 20 p.e), while the high-gain amplifier saturates for high-intensity signals (above 200 p.e.). The bottom panel shows the ratio between HG and LG channels outputs. The intensity range where both LG and HG channels are linear (between 30 and 200 p.e.) is used to determine the HG/LG ratio, which is an important input parameter for calibration (§4).

Trigger From the technical point of view, it would be very difficult and power-consuming to have the camera taking data continuously all the time. It is far more efficient to have the camera *trigger* only when a flash of Cherenkov light reaches it. The system which achieves that is simply called “*trigger*”. Its role is to provoke the digitization and readout of all the PMT output pulses when a given set of criteria are fulfilled.

There are different levels of trigger, each corresponding to a given criterion and a different scope. How these different levels are called and implemented can vary from one experiment to

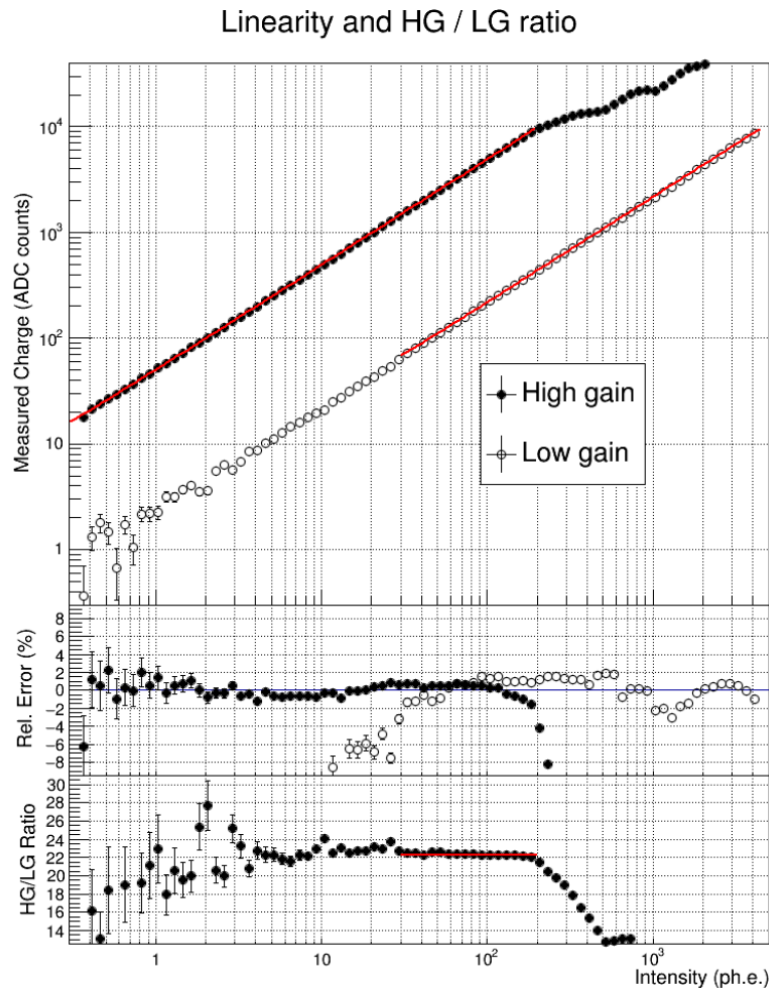


Figure 13: Measured charge after amplification measured in the LG and HG channels (top panel) for H.E.S.S. small telescope post-upgrade cameras. The HG channel starts to saturate for an input signal of ~ 200 p.e. The LG channel is not linear anymore below ~ 30 p.e., as can be seen from the plot in the middle panel showing the relative error between data points and linear fits. The HG/LG ratio is determined from the range where both channels are linear (red horizontal line, bottom panel). Figure adapted from [15].

another, and we will give the example of how the trigger of H.E.S.S. CT5 works. Three levels are used.

The first one is at the pixel level and is called L0. To trigger at level L0, the charge in a given pixel must exceed 4 p.e. This value for the threshold is used for all pixels. It is determined on a test bench by studying how the L0 trigger rate varies as a function of the threshold setting when the camera is illuminated by a constant white light simulating the NSB. For a very low threshold, all pulses give a positive trigger. Increasing the threshold allows to select less and less of the NSB photons, but at some point, another contribution starts to dominate, due to the PMT after-pulses (see §3.2). The value for the threshold is selected just below the break of the curve (Figure 14).

The second level is the *camera trigger*, called L1. The corresponding criteria is based on the fact a Cherenkov shower usually illuminates several contiguous pixels at the same time. For

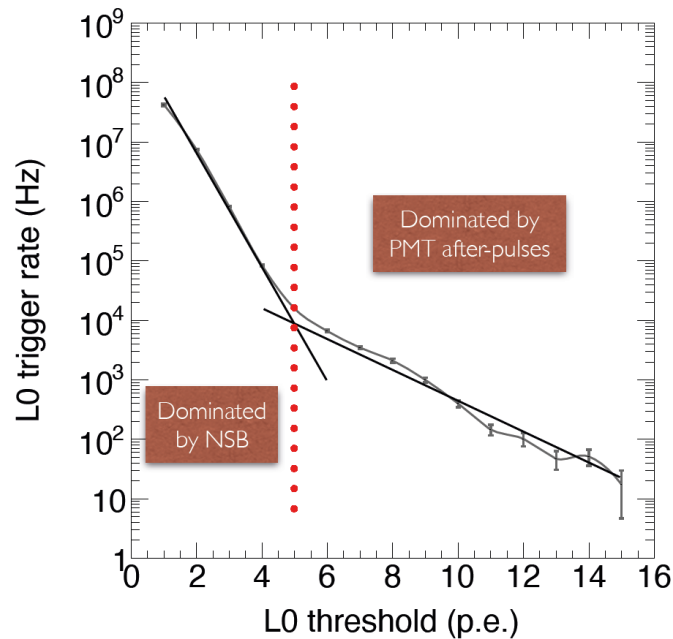


Figure 14: The L0 trigger rate (in Hz) as a function of the charge L0 threshold. Two contributions are clearly visible. The one on low values of the threshold is dominated by NSB, while the other is dominated by PMT after-pulses. Figure from [10].

example, in the H.E.S.S. CT5 camera, L1 requires a number ≥ 3 of close-by pixels fulfilling the L0 criteria. When this condition is met, the readout of all pixels starts. The point is that the L1 trigger decision takes some time, roughly 200 ns. During this time, the signal are stored in memories.

The L2 trigger is generated at the array level by a system called “*central trigger*”, taking into account the L1 trigger signals issued by the five cameras. CT5 being much bigger than the other telescopes, it triggers alone most of the time (for $\sim 75\%$ of the events). In that case, the central trigger simply accepts the event, and tags it as being a *monoscopic event*. When two telescopes or more trigger within 80 ns, the central trigger tag the event as being a *stereoscopic event*. Another goal of the central trigger system is to provide each event with a unique number, the “*event number*”.

To close this paragraph about trigger, let us point out that cameras usually have different modes of trigger for different purposes. The *internal trigger* is used for regular data taking. The *external trigger* is used so that the trigger signal can be provided by an external device. It is used for specific calibration data-taking procedures (or *runs*) such as single photo-electron runs⁸ (§4). Last, a software-generated trigger or *soft trigger* can be generated by the camera control software. It is mainly used for the warm-up and testing of the camera electronics.

Analog memories The use of memories to store PMT signals is necessary because the L1 trigger decision is not instantaneous. As already mentioned above, the L1 decision takes around 200 ns. This time corresponds to the electric signal propagation along cables from the drawers to the L1

⁸They are different types of runs, as will be discussed in §4. They are of different duration. A single photo-electron run is usually 2 minutes long, while a data-taking run lasts for 28 minutes.

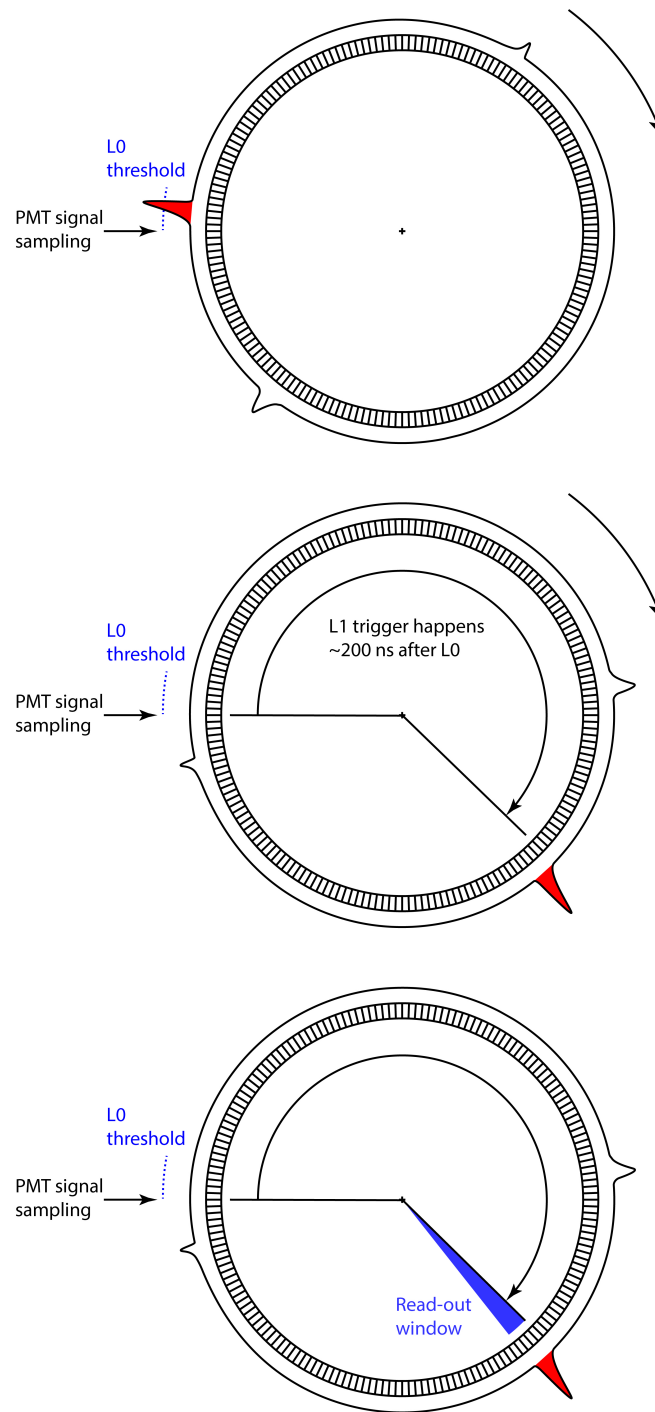


Figure 15: Principle of circular memory buffer usage for H.E.S.S. cameras. Top: the anode signal of a PMT exceeds the L0 threshold (red pulse). Middle: assuming other pixels have also issued a L0 trigger, the L1 trigger signal is generated. L1 trigger decision takes ~ 200 ns. In the meantime, the red pulse has been shifted in the memory buffer as new samples were recorded. Bottom: for each pixel (or channel), it is necessary to know where the pulse is in the memory so that the corresponding samples (the blue sector) are read-out. The corresponding shift is stored in a database for each channel.

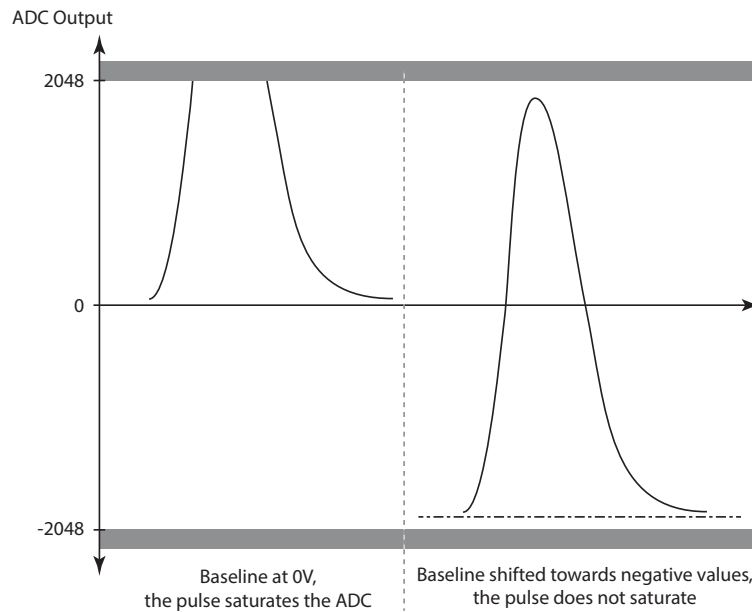


Figure 16: The baselines of the signals are shifted to negative values to avoid ADC saturation and to use the full ADC range. Left: With no shifting, a large amplitude pulse can saturate the ADC. Right: A pulse with the same amplitude, but with a shifted baseline (dash-dotted line) does not saturate the ADC.

trigger electronics, to the signal processing, and to the propagation of the trigger decision back to the drawers.

In H.E.S.S., switch capacitor memories are used. The amplified input signals (HG and LG) are sampled at a rate of 1 Giga-Samples per second and each sample is stored as an analogue voltage by charging a capacitor. For the CT5 camera, the memory chip (called SAM for *Swift Analogue Memory*) has 256 capacitors and so can store up to 256 samples, corresponding to 256 ns of signal. It is configured as a circular buffer, meaning the content is fully overwritten every 256 ns. Figure 15 gives a simplified view of how memories are used, from the reception of a L0 trigger to the read-out.

During the time needed for L1 trigger decision-making, signal acquisition continues and more PMT pulses can be recorded. Considering the circular buffer has 256 cells, it can be pointed out that most of the memory is filled while waiting for the L1 trigger decision. Moreover, for each memory chip (one for each PMT), and because each chip is slightly different, the delay necessary to receive the L1 decision will also be a little bit different. Different delays result in different shifts between the actual position of the pulse in memory (including the ones that triggered the camera) and the position where it is expected to be found. As a result, the readout process needs to be carefully calibrated for each drawer so that the values of the shifts are known for each analogue memory chip.

Because it is not possible to write and read the memory content at the same time, when a L1 trigger is received, analog memories stop acquiring new samples. The number of samples which are read out (16 in the case of the H.E.S.S. CT5 camera) is chosen so that the entire PMT pulse is captured. The shifts mentioned previously are taken into account to set the beginning of the read-out window, ensuring the PMT pulse is entirely contained inside of it. The read-out is done for HG and LG channels for all PMT, including the ones which did not participate in the trigger. Then,

the analogue signals (a value of a voltage for each sample) are digitized by an ADC (Analogue to Digital Converter), i.e. converted into a digital integer number, expressed in ADC counts, in the range ± 2048 . In order to use the full range of the ADCs, the baseline of the signal is shifted towards negative values (Figure 16). ADC conversion takes time, around $250 \mu\text{s}$ for a full event. This is the reason why signals are digitized only when the L1 trigger criterion is met.

FIFO (First In First Out) memory buffers are used all along the signal path to make the tasks of analog memories and of the rest of the Data Acquisition (DAQ) system independent as it helps reducing the *dead-time* (the time during which the camera cannot process any new event), to $15 \mu\text{s}$ and make it much smaller than the read-out time.

To end this section, let us go back to Figure 12 for a moment. We have reviewed most of the elements which are present in the figure and how they are used: amplifiers, analogue memories, ADC and FIFO memory buffers. There are still a few items we did not cover. Active bases manufactured by ISEG⁹ are used to power the PMT and monitor the current (HVI) drawn by each one of them. HVI monitoring allows to detect high luminosity on a given pixel, e.g. because of a star. In extreme cases, pixels can be switched off to protect the PMT. FPGA (Field-Programmable Gate Array) are electronic components which can be programmed to perform some specific tasks. In the case of the CT5 camera drawer, FPGA is used to receive the L1 trigger signal, start the read-out of analogue memories and digitization. More importantly, they also compute the HG and LG charges by integrating digitized PMT signals. These charges are obtained by summing ADC counts, and so they are expressed in ADC counts as well. Finally, the *Slow Control* is used to monitor and control the drawer. Slow control data is intertwined with raw data and gathers various parameters (high voltages, high voltage currents, temperatures) which are used to ensure proper working conditions. The slow control data is recorded every ~ 1000 events. The FPGA on the Slow Control board is also used to encapsulate the data and transmit it from the drawer to the camera electronics, and then to the array data pipeline.

3.3.3 Summary

After this lengthy dive into some technical details of how a Cherenkov telescope camera works, we are at a point where we can understand what *raw data* actually are and how they are obtained. For each event, and so for each camera trigger, raw data consists of two values of the charge, one for high gain and one for low gain amplification, obtained by integrating anode pulses (16 samples). The charge is expressed in ADC counts, a digital number in the range $\pm 2048 \times 16 = \pm 32768$. In the next section, we will see all the steps necessary to go from this digital value back to a charge expressed in photo-electrons, and to a number of Cherenkov photons (or Cherenkov light intensity).

⁹<http://iseg-hv.com/en>

4. Calibration

4.1 Overview

Calibration is a multi-step process during which charges expressed in ADC counts are converted back to p.e. The primary ingredient for that is charge distributions, which are obtained from low gain (LG) and high gain (HG) channels for each pixel. An additional step is used to get the Cherenkov light intensity for each event. Calibration requires data to be taken in different specific conditions. The corresponding runs are called “*calibration runs*”.

The first step is used to recover the baseline of the signal in each pixel and both gains. The corresponding run is referred to as “*pedestal run*”: the baseline is the pedestal on top of which lies the signal. The second step is used to assess the gains in the HG channel, which in turn allows to convert ADC counts to p.e. “*Single p.e. runs*” (SPE) are used for that. Gains in the LG channel cannot be retrieved with that method, but they can be deduced from the HG knowing the *HG/LG ratio*. This ratio can be evaluated directly from regular data-taking runs. The third step is used to correct for non-uniformities between pixels. This is the so-called “*flat-field*”. It can indeed happen that the same amount of light does not give the exact same charge, because two PMTs can have different QE, or because one of them is slightly covered by dust while the other is cleaner¹⁰. The last step is used to assess the *optical transmission efficiency*, i.e. allowing the conversion from charges to Cherenkov light intensity. This parameter, in addition to other atmospheric monitoring quantities, is used as an input for detailed Monte Carlo simulations.

4.2 Pedestal

The first step of calibration is to get the baseline of the signal, the *pedestal*. This is done using charge distributions obtained when the pixels do not receive any light, either in dedicated runs or using non-illuminated pixels in regular data-taking runs. In these conditions, the charge distributions are Gaussian. The position of the pedestal, corresponding to the charge distribution average, depends directly on the signal baseline (a voltage). It is a choice made when the electronics is designed (see Figure 16 and the corresponding explanations), but it can vary slightly from one channel to another. In addition, the pedestal width (standard deviation) depends on the amount of electronic noise. The noisier the channel, the wider the pedestal distribution. The maximum amount of noise, and so the maximum pedestal width is usually amongst the technical requirements which have to be complied with when designing a camera.

The pedestal can be assessed using two different methods. On one hand, one can take dedicated runs to record the baseline with the camera lid (the protecting plate that covers the camera) closed so that there is no external light falling onto the PMTs. A random trigger is used instead of the internal trigger since in those conditions the signal do not meet the L0 trigger criterion. Figure 17 shows the corresponding charge distributions for the LG and HG channels. During the calibration step, these distributions are fitted with Gaussian functions to extract the baseline (the mean) and the pedestal width (the standard deviation). These parameters are stored in a database to be used later on.

¹⁰In modern designs, the camera is often sealed and put under a slight over-pressure so that dust cannot enter. In that case, the cooling of the electronics requires more complex systems.

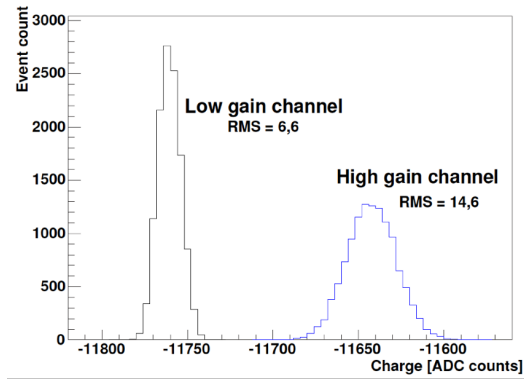


Figure 17: Charge distribution obtained from dedicated runs in the case the camera is in the dark (lid closed). Distributions are Gaussian and correspond to the baseline of the signals, i.e. the pedestal. Figure from [3].

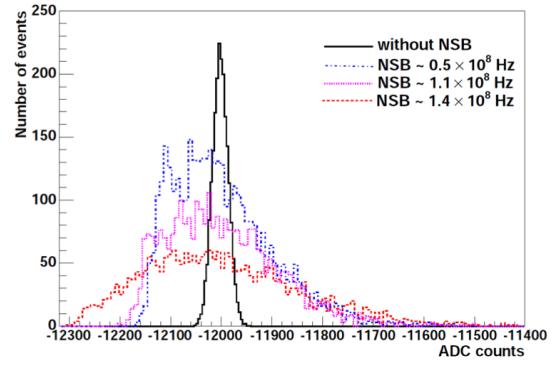


Figure 18: Charge distributions obtained with regular data-taking runs for pixels which are not hit by Cherenkov light. The case with no NSB corresponds to the narrower Gaussian distribution (black curve), the higher the NSB is, the wider the distribution. Figure from [16].

On the other hand, data taken during normal observation runs can be used. In that case, only the pixels with no Cherenkov signal are considered. However, these pixels can still be illuminated by NSB photons. The NSB results in wider charge distributions which are no longer Gaussian. Figure 18 shows how the charge distributions look like for different NSB rates. The rates are expressed in p.e. per second, which corresponds simply to Hertz.

As a consequence, the study of pedestal width can be used to produce a map of the NSB. Figure 19 (top) is an example of such a map produced from pedestal widths, showing the Galactic Centre region. The bottom picture shows the optical emission in the same part of the sky. There is a clear correlation between the NSB evaluated from pedestal widths and the optical emission, illustrating that the NSB is due to bright regions in the sky, mainly due to stars.

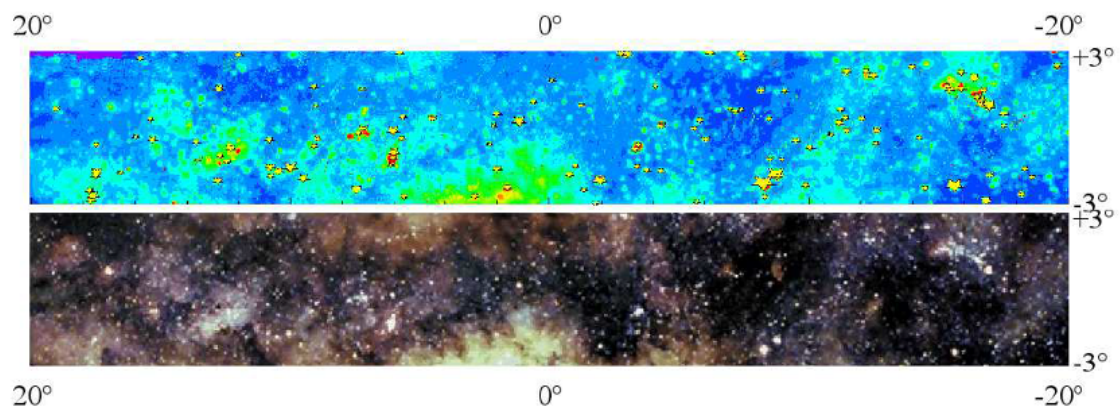


Figure 19: The Galactic Center region map obtained from pedestal width (top), and from optical observations (bottom). Bright regions of the sky give a high NSB rate, which results in wider pedestals. On the top picture, yellow stars indicate stars with a magnitude lower than 7. Figure from [3].

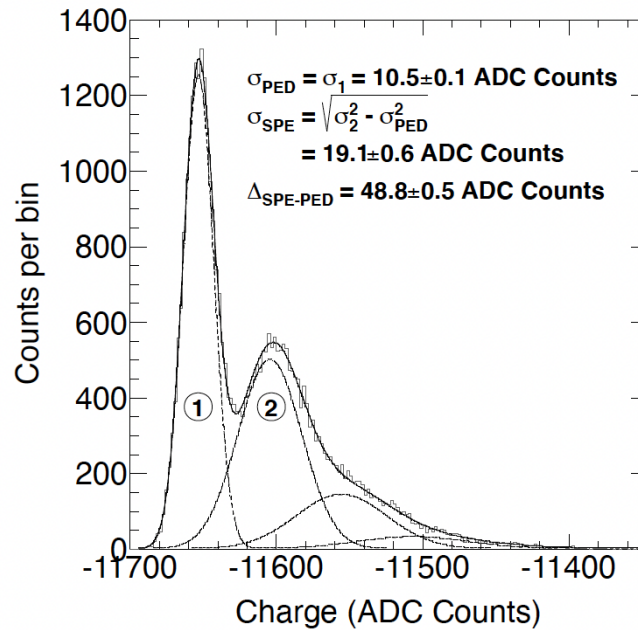


Figure 20: Charge distribution obtained for one pixel during a run where the illumination is low enough so that on average 1 p.e. is produced at the photocathode. Peak number 1 corresponds to the pedestal (baseline and electronic noise). The corresponding standard deviation is given on the plot (σ_{PED}). Peak 2 corresponds to the single p.e. Another contribution above -11500 ADC counts can be seen corresponding to the cases where 2 p.e. are produced. Figure from [10].

4.3 Gain calibration

Once the baseline of the signal is reconstructed, the next step is to measure the overall *gain* related to the PMTs and amplifiers. Strictly speaking, the gain should simply be a multiplication factor. However, here it represents the number of ADC counts per p.e., meaning it also includes the conversion factor of the ADC. As already discussed earlier, the gain is different for the HG and LG channels and allows the conversion between ADC counts and photo-electrons.

HG values are obtained from dedicated runs (called “*Single photo-electron*”, “*Single p.e.*” or SPE runs). Specific runs are necessary since data-taking with a very low amount of light is needed. The camera with opened lid, protected from any ambient light, and with PMTs at their nominal high voltage values is illuminated by light flashes. The intensity of the flash is carefully adjusted so that on average 1 p.e. is produced at the photocathode. Since the amount of light is very low, most of the light pulses give no signal and the charge distribution shows only the pedestal contribution. When 1 p.e. is produced, another contribution to the charge distribution will appear as a second peak (Figure 20). For this type of run, the L0 trigger criterion is not fulfilled and the camera needs to be triggered by an external source. This is usually done with the same pulse generator which also provides the light flashes.

Figure 20 also illustrates how the *gain* is extracted from the distribution. A fit is performed using a sum of several Gaussian peaks, weighted by a Poisson law. The gain is the parameter noted $\Delta_{\text{SPE-PED}}$ on the plot because it corresponds to the difference between the SPE peak and the position

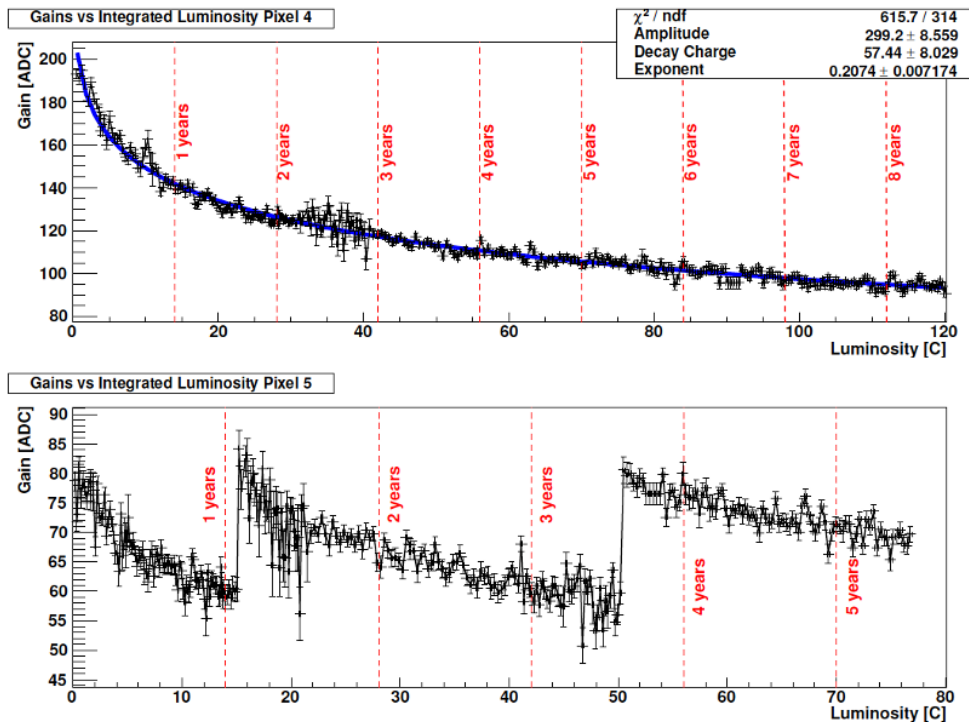


Figure 21: Top: time evolution of the gain measured on a test bench for one particular pixel showing the effect of the ageing. The X axis gives the integrated luminosity expressed as a charge in Coulombs. Bottom: time evolution of the gain for one particular pixel of a small camera on the H.E.S.S. site. Sharp edges correspond to the times when the high voltage of that pixel was adjusted to compensate for the PMT ageing. Figure from [3].

of the pedestal. Here the gain is found to be 48.8 ± 0.5 ADC counts per p.e.

During calibration, the values of the gains are obtained for each pixel and stored in a database. SPE runs are repeated on a regular basis to monitor the evolution of the gain in time. An important but unpreventable fact is indeed that PMTs are subject to ageing, which translates into the gain decreasing with time. The top panel of Figure 21 shows the long-term evolution of the gain for one particular pixel of a H.E.S.S. camera test bench. This test was performed using a quite large amount of light so that a few hours only were necessary to simulate an equivalent continuous observation time of 8 years on the H.E.S.S. site. The decrease in the gain due to PMT ageing is clearly visible. On site, high voltage adjustments are made from time to time to re-adjust the gains to the nominal value¹¹. The bottom image in Figure 21 shows the on-site evolution of the gain for one particular pixel of a H.E.S.S. small camera. The nominal value of the gain is 80 ADC counts per p.e. The sharp edges on the plot correspond to the times when high voltage values were increased to compensate for the ageing of the PMTs.

Because the amount of light necessary to have 1 p.e. is very low, the SPE peak in the charge

¹¹Adjusting the gain of the amplifiers or the ADC conversion factor is not possible once the design of the electronics is done. The only way to change the gain is to change the PMT high voltage (§3.2).

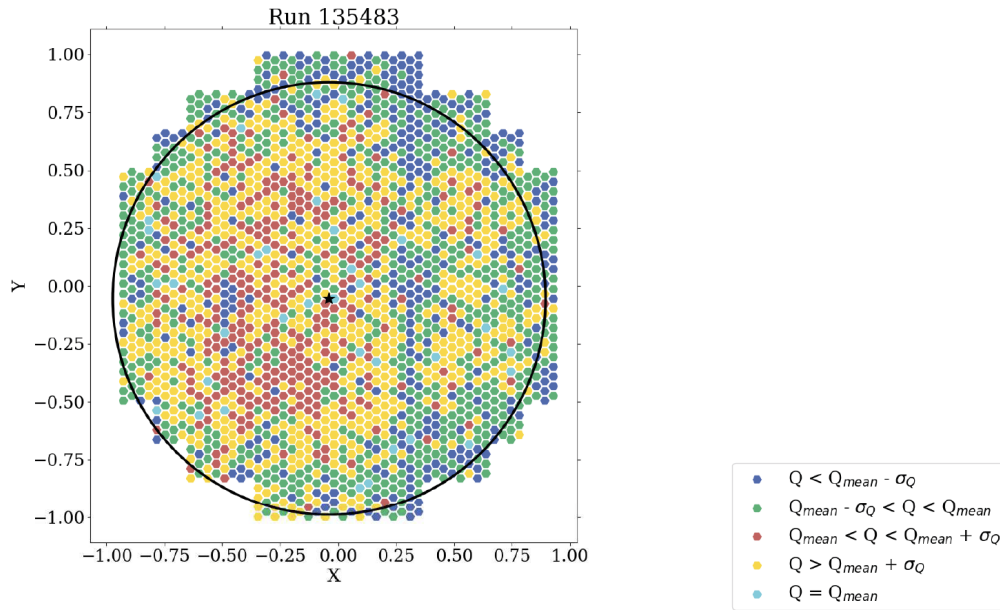


Figure 22: Collected charge obtained from a particular flat-field run taken with the H.E.S.S. CT5 camera. The different colours correspond to different ranges of the charge. The ranges are defined from the average charge value Q_{mean} and its standard deviation σ_Q . The black circle corresponds to the reconstructed position of the light spot, showing a small offset with respect to the camera center. Figure from [17].

distribution cannot be resolved in the low gain channel. The value of the gain for the LG channel is instead deduced from the HG gain by using the HG/LG ratio (see §3.3.2 and Figure 13). The HG/LG ratio can be extracted from regular data taking, no specific run is needed. Here again, the values of the HG/LG ratios are stored in a database.

4.4 Flat-field

As we have seen, pedestal and gain calibration allow to convert between ADC counts and charges in p.e. However, there are other instrument-related characteristics which can result in different PMT output signals even when they receive the same amount of light: Winston cone reflectivity, and PMT collection and quantum efficiencies (§3.2). To take this into account, “flat-field” runs are performed during which the camera is illuminated by a very uniform light source (hence the name flat-field). For H.E.S.S., this light source is located at the center of the primary mirror. From the charge collected in each pixel (Figure 22), and comparing this charge to the average one, a cross-calibration coefficient (also called *flat-field coefficient*) is attributed to each pixel, and stored in a database.

4.5 Summary: from ADC counts to a charge in photo electrons

The dedicated calibration runs we have mentioned so far are used to get several different parameters: pedestal in HG and LG (which we will note P_{HG} and P_{LG}), gain in the HG channel (γ_{HG}), HG to LG ratio (HG/LG), and flat-field coefficients (FF). From these parameters, we can convert ADC counts in the LG and HG channels (noted ADC_{HG} and ADC_{LG}) to a number of photo

electrons, noted S_{HG} and S_{LG} :

$$S_{HG} = \frac{ADC_{HG} - P_{HG}}{\gamma_{HG}} \times FF \quad (1)$$

$$S_{LG} = \frac{ADC_{LG} - P_{LG}}{\gamma_{HG}} \times \frac{HG}{LG} \times FF \quad (2)$$

The charge in p.e. will be the main ingredient of the next steps of data analysis. However, calibration includes an additional step, which is used to evaluate the optical efficiency of the telescopes.

4.6 From a charge to Cherenkov light intensity

As the reader will realize later, the reconstruction and analysis step (§5) makes heavy use of Monte Carlo simulations. These simulations are essential to ensure all characteristics of the detector are properly understood. They include cascade generation and development, Cherenkov photon production, propagation, collection by the main mirror, and detection by PMTs. Trigger and electronics responses are also taken into account to generate simulated raw data in the same format as actual (real) raw data.

The simulations need to be as accurate as possible as regard atmosphere transparency, mirror and Winston cone reflectivity, and PMT collection and quantum efficiency¹². To achieve this accuracy, it is necessary to evaluate the optical efficiency, which is in turn used in the simulations to relate the Cherenkov light intensity to the charge in p.e.

The overall optical efficiency is given by

$$\text{Optical Efficiency} = R \times (1 - S) \times C \times (QE \times CE), \quad (3)$$

where R is the mirror reflectivity integrated over wavelength ($\sim 80\%$), S takes into account the shadow of the camera and its support masts on the mirror ($\sim 10\%$), C corresponds to the camera collection efficiency (photon lost between the mirror and the camera, and due to the Winston cone reflectivity, $\sim 70\%$) and $QE \times CE$ is the PMT efficiency ($\sim 30\%$). With these values, the optical efficiency is $\sim 15\%$.

Atmospheric muons are used to get the overall optical efficiency as they offer natural calibration beams with several advantages:

- Their radiation spectrum is very similar to the Cherenkov emission from gamma-ray showers.
- They reach the ground as they are ultra-relativistic, making the light yield independent of the muon energy and only depending on the track length.
- Their signal is very short in time.

Muons also probe the atmosphere transparency, but only on the part of the track which can be seen by the primary mirror. H.E.S.S. small telescopes can detect the last ~ 400 m of a muon track while the CT5 telescope can detect the last ~ 700 m.

Figure 23 shows the distinctive shapes that muons give with a Cherenkov telescope for simulated and real data. These particular footprints are called “muon rings”.

¹²Note that all these parameters depend on the wavelength.

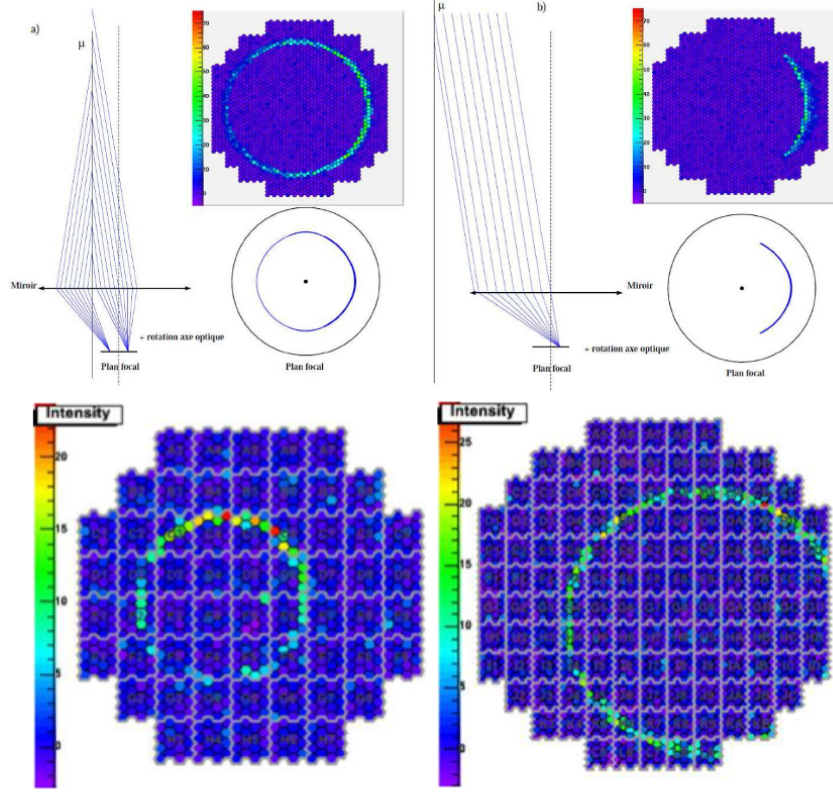


Figure 23: Top row: simulated images obtained from muons depending on the angle of incidence and impact location. Left: the muon track is parallel to the optical axis, and hit the main mirror. Right: the track is parallel to the optical axis, but it falls out of the mirror. On the bottom line are shown two examples of muon ring images recorded by H.E.S.S. Figures from [16].

For a given muon track, the number of photons reaching the camera per unit wavelength (λ), azimuth angle (ϕ) in the camera plane, and track length (l) is given by:

$$\frac{d^3 N}{dl d\phi d\lambda} = \frac{\alpha}{2} \sin(2\theta_c) \frac{\psi(\lambda)}{\lambda^2} D(\phi, \rho) a(l, \lambda), \quad (4)$$

where the sinusoidal term $\sin(2\theta_c)$ is related to the radius of the muon ring and where $\psi(\lambda)$ is the optical efficiency at wavelength λ . The term $D(\phi, \rho)$ depends on the geometries of both the muon track and the optical system, and $a(l, \lambda)$ corresponds to the atmospheric absorption. This parameter a is mainly related due to dust and aerosol absorption. It can be evaluated from models of atmosphere, and can also be deduced from measurements with a LIDAR (Laser Imaging Detection and Ranging, see e.g. [18]). By selecting muon rings observed in the data, and by comparing these rings with the model of Eq. 4, it is possible to deduce parameter $\psi(\lambda)$.

Figure 24 shows the long-term monitoring of the optical efficiency for the four H.E.S.S. small telescopes, as deduced using the muon ring technique. It is decreasing with time due to dust slowly covering mirrors, Winston cones and PMTs. It increases when PMTs are cleaned, when Winston cones are replaced, or when mirrors are refurbished.

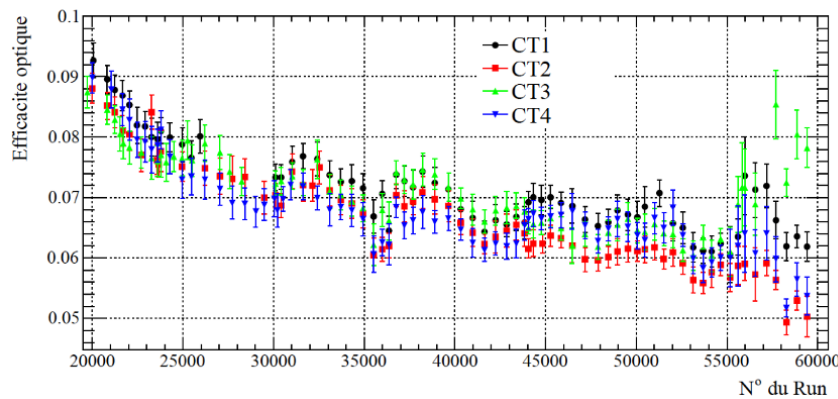


Figure 24: Optical efficiency, for the four small H.E.S.S. telescopes. Each point corresponds to the average optical efficiency over a month and for all pixels. The optical efficiency decreases with time. The large increase for CT3 (right end side) is due to its mirror being refurbished. From time to time, a smaller increase is seen, due to the increase of PMT high voltages. Figure from [19].

4.7 Summary

At the end of the calibration step, we obtain for each pixel a charge in p.e. as well as a way to assess Cherenkov light intensity for simulation purposes. These quantities will be the main ingredients for the next step: reconstruction and analysis.

Before switching to that topic, it is important to note two important additional points about the calibration process. Calibration is the first step of data analysis. As such, it gives the first opportunity to have a close look at data quality. As an example, inoperative pixels or other hardware problems are usually identified at the calibration step. This information will be used later in the reconstruction and analysis steps. Faulty pixels can result in biases in energy reconstruction if they are not removed from the analysis. As a result, development of calibration software requires extreme care.

5. Reconstruction and analysis

Before we dig into the details, let us discuss the vocabulary and give some basic definitions. The starting point of reconstruction is an image provided by a camera after the calibration step. We saw earlier that for a particular event, the charge in p.e. is obtained for each pixel and each gain. The word “*reconstruction*” is straightforward: its goal is to extract (reconstruct) some information from calibrated data sets:

- The energy (reconstructed energy, not to be confused with the true energy).
- The direction of the incoming primary particle.
- Its impact location on the ground.
- A numerical quantity giving an indication on the nature of the primary particle. This number is called a “*discriminating variable*”.

On the other hand, the use of the word “*analysis*” can be confusing. After all, calibration and reconstruction are part of data analysis. Used together with reconstruction, the word “*analysis*” refers to the astrophysical source which is observed. The analysis step comes after the reconstruction. Its goals are to:

- Estimate the background as precisely as possible.
- In case the signal is not significant with respect to the background, it is possible to give an upper bound on the flux, taking into account the performance of the instrument.
- In case the signal from the source is significantly more intense than the background, a detection can be claimed, and parameters *of the source* can be extracted: true energy distribution (spectrum), time distribution (light curve), size and shape of the emitting region (morphology).

A critical element of both reconstruction and analysis is the Monte Carlo simulation of the experiment. A dedicated software is used to simulate primary particles (photons, electrons, hadrons), the cascades they produce in the atmosphere, the Cherenkov emission, the propagation and absorption of Cherenkov photons in the atmosphere, their reflection on the primary mirror and their detection by the PMT. The electronics is also modeled: amplifiers, trigger system, etc. At the end, the simulation software allows to obtain simulated raw data. Calibration, reconstruction and analysis can then be run in the same way on simulated and real data, allowing to compare both outputs. This comparison is done on a regular basis, using well known sources (e.g. the blazar PKS 2155-304, or the Crab nebula), in order to check that the way the detector work is in agreement with expectations. Any deviation between simulated and real data would need to be understood. It could indeed indicate a possible bug in the calibration, reconstruction or analysis software. For completeness, let us mention that it is crucial to consider the atmosphere’s properties in simulations. This can be achieved either by constructing a model of the atmosphere or, as seen earlier, by measuring its characteristics directly using a LIDAR.

Analysis and reconstruction are preceded by some additional steps. For a given source, data sets usually consist in several data taking runs, but it can happen that some of these runs are of poor quality, because of technical problems, or because of variable atmospheric conditions (e.g. a cloud entering the field of view). So, data quality checks are performed, leading to the selection of good quality runs. Only good quality data is reconstructed and analysed.

5.1 Reconstruction

As previously mentioned, the goal of the reconstruction is to determine the direction, the point of impact on the ground, and the energy of the primary particle. It also provides a way to discriminate the nature of primary particles (hadron-like or gamma-like). Remember also that a GPS clock is used to attribute a very precise time stamp to the event as soon as it is triggered (§3.3.2).

Two main methods are currently used for reconstruction: the Hillas [5] and the Model [6] methods. The Hillas reconstruction method is older and was developed in the early 1980s for the Whipple experiment (see e.g. [20]). The technique was continuously improved since it was first proposed, and it is still widely used, mainly due to its simplicity.

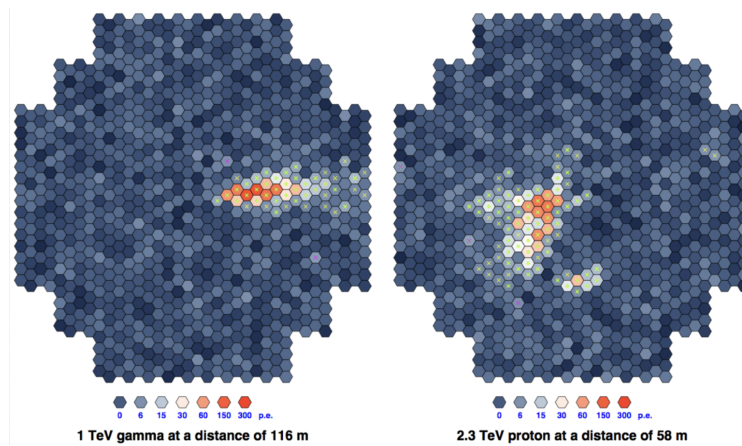


Figure 25: Left: image in the camera of a photon-induced shower. Right: image in the camera of hadron-induced shower. The gamma shower image is quite elliptical in shape, while the hadronic shower image shows multiple sub-clusters. The color scale corresponds to charge expressed in p.e. Energies and impact parameters are given at the bottom of each plot. Courtesy of S. Ohm.

On the other hand, the Model reconstruction method is a more sophisticated approach. Showers are modeled with high accuracy with different input parameters (energy, zenith angle, etc.), and then compared to the actual measured showers to create a mapping between the two. From that mapping, the parameters of the detected showers are derived.

Other, more complex techniques, relying, for example, on the use of decision trees or neural networks have also been developed. They usually show better performance, but they can be challenging to implement. They are not discussed in these notes, but the interested reader will find more on this in the literature (see e.g. [21]).

5.1.1 Hillas reconstruction

Basic principles Hillas reconstruction relies on the fact that the image induced by a gamma-ray has a relatively regular and elliptical shape. On the contrary, images obtained from hadronic showers are irregular and often show multiple clusters (Figure 25).

Images are first cleaned (see the next paragraph), before being fitted with an ellipse. The corresponding *Hillas parameters* are depicted in Figure 26 and are defined as follows:

- L - length of the ellipse.
- W - width of the ellipse.
- $Size$ - total image amplitude in p.e.
- d - nominal distance (the distance of the centre of the ellipse to the centre of the camera).
- φ - the azimuthal angle of the image main axis.
- α - orientation angle.

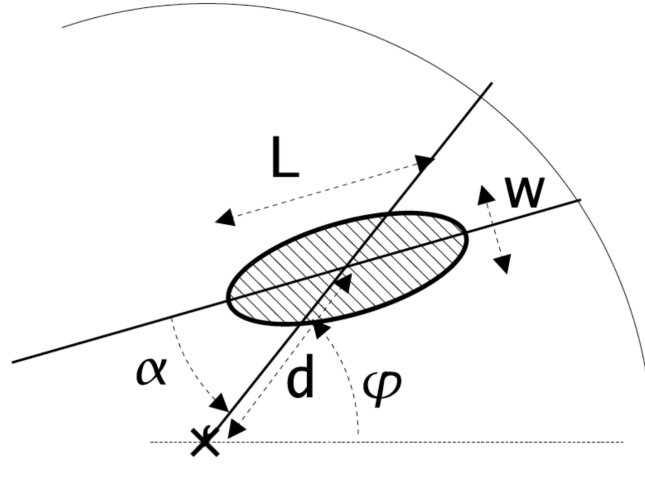


Figure 26: Definition of Hillas parameters. The cross at the bottom represents the centre of the camera. Figure from [3].

Each of these parameters can be obtained from the image using the intensity q_i (in p.e.) and position (x_i, y_i) of each pixel with index i . Additionally, several quantities, such as averages and standard deviations, are computed:

$$\begin{aligned}
 \langle x \rangle &= \frac{\sum_i x_i q_i}{\sum_i q_i}, \\
 \langle y \rangle &= \frac{\sum_i y_i q_i}{\sum_i q_i}, \\
 \langle xy \rangle &= \frac{\sum_i x_i y_i q_i}{\sum_i q_i}, \\
 \langle x^2 \rangle &= \frac{\sum_i x_i^2 q_i}{\sum_i q_i}, \\
 \langle y^2 \rangle &= \frac{\sum_i y_i^2 q_i}{\sum_i q_i}, \\
 \sigma_{y^2} &= \langle y^2 \rangle - \langle y \rangle^2, \\
 \sigma_{x^2} &= \langle x^2 \rangle - \langle x \rangle^2, \\
 \sigma_{xy} &= \langle xy \rangle - \langle x \rangle \langle y \rangle.
 \end{aligned} \tag{5}$$

From these, we can define some other variables that we will use later:

$$\begin{aligned}
 \chi &= \sigma_{x^2} - \sigma_{y^2}, \\
 z &= \sqrt{\chi^2 + 4\sigma_{xy}}, \\
 b &= \sqrt{\frac{(1 + \chi/z)\langle x \rangle^2 + (1 - \chi/z)\langle y \rangle^2 - 2\sigma_{xy}\langle x \rangle \langle y \rangle}{2}}.
 \end{aligned} \tag{6}$$

Finally, we obtain a way to deduce Hillas parameters from the content of the image:

$$\begin{aligned}
 d &= \sqrt{\langle x \rangle^2 + \langle y \rangle^2}, \\
 L &= \sigma_x^2 + \sigma_y^2 + z, \\
 W &= \sigma_x^2 + \sigma_y^2 - z, \\
 \alpha &= \arcsin\left(\frac{b}{d}\right).
 \end{aligned}
 \tag{7}$$

Image cleaning The first step of Hillas reconstruction is image cleaning. Its goal is to keep only the image of the shower of interest while suppressing other background signal which may be present in the camera. The NSB is a significant source of noise which need to be suppressed.

To achieve this, a two-step process is typically used, using two different thresholds. The first threshold, s_1 , is applied to all pixels in the image. Only the pixels with a signal above s_1 are retained. However, since the NSB (stars) can sometimes generate signals above s_1 , a second threshold, s_2 , is applied to filter out isolated signals. A pixel above the s_1 threshold is kept only if it has at least one neighbour with a signal above s_2 .

The choice of threshold values s_1 and s_2 depends on the level of the NSB present in the camera, which can vary depending on the location in the sky being observed. For instance, observing Galactic sources would result in a higher NSB, as there are many stars in the galactic plane that contribute to the background. In contrast, observing extragalactic sources usually result in a lower NSB.

Figure 27 shows two examples of image cleaning, with two different choices for the thresholds. The plot at the center shows the result of the cleaning with $s_1 = 4$ and $s_2 = 7$. The plot on the right shows the result of the cleaning of the same image with more stringent values of $s_1 = 5$ and $s_2 = 10$. It can be noticed that some clusters remains with the loose cuts while they disappear with the stringent cuts.

If the selection cuts are too loose, the cleaning may retain clusters of pixels. This can lead to the mis-identification of the event as an hadronic event. On the other hand, a cleaning with too stringent

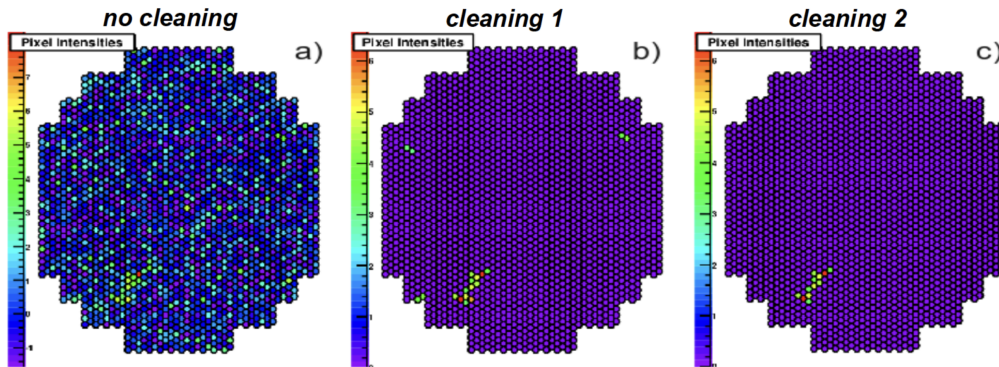


Figure 27: Left: the image of an event with no cleaning. The NSB contribution is clearly visible and it is difficult to identify any shower. Center: result of the cleaning for $s_1 = 4$ and $s_2 = 7$. Right: result of the cleaning with $s_1 = 5$ and $s_2 = 10$. The small clusters that are still there with the first cleaning cuts disappear with more stringent thresholds. Courtesy of S. Ohm.

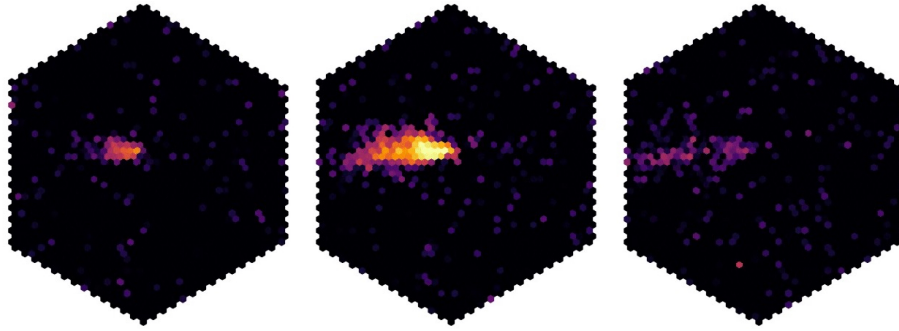


Figure 28: Images of the shower development induced by a gamma ray at three different times (from left to right). These images were recorded by the new camera of the CT5 H.E.S.S. telescope, NamCAM. Credit: H.E.S.S. Collaboration.

cuts can make a hadronic shower image resemble a gamma-ray image. Therefore, the cleaning process must be carefully adjusted and calibrated to ensure optimal performance and accuracy in event identification.

Degeneracy on the source direction An ellipse is symmetric with respect to its minor axis. For reconstruction using only one telescope (monoscopic observation), this translates into the fact the direction of the source is degenerate: on the left panel of Figure 26, the incoming gamma-ray could come from the right or from the left. However, a closer look at the image give us a clue on the direction of propagation of the shower on the camera plane. It can be seen that the left part of the image is sharper than its right part, which looks more diffuse. Reconstruction software are developed so that they are able to exploit this feature.

Alternatively, most recent camera designs allow the use of timing information in image analysis. They can resolve cascade development as a function of time, further enhancing the accuracy of the reconstruction of the direction. In this scenario, the top and bottom of the cascade can be clearly identified, and the direction of the source can be easily reconstructed (Figure 28).

In the case of hadronic showers, muon rings can be easily isolated and analysed by selecting the appropriate time frames (Figure 29). The gamma-hadron separation can then be improved.

Both figures 28 and 29 were extracted from animated GIF files which can be seen online¹³.

Use of stereoscopy If we transition from a single telescope to an array of several telescopes, the determination of the source position becomes more precise. Stereoscopy is a technique that involves observing the same shower from multiple positions simultaneously. The distance between the small telescopes is 120 meters for the H.E.S.S. array, and each telescope is at a corner of a square. This arrangement results in four images of the same shower (Figure 30, left). These images can be merged on a single (virtual) camera plane (Figure 30, right). After fitting ellipses to each individual camera image, the results are combined. This combination provides the source location, which is the point where the reconstructed major axes intersect. Knowing exactly where the telescopes are pointing at (see the paragraph about pointing below), it is then possible to deduce the source location in the sky, usually expressed using right ascension (RA) and declination (DEC) coordinates.

¹³<https://www.mpi-hd.mpg.de/hfm/HESS/pages/home/som/2020/10/>

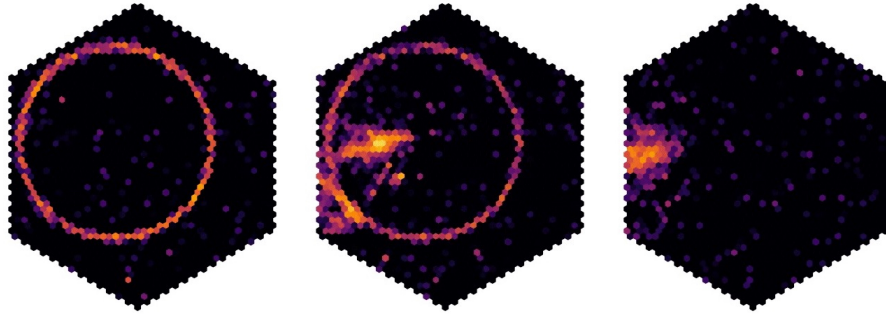


Figure 29: Images of the shower development induced by a hadron at three different times (from left to right). It can clearly be seen that the muon ring appears before the rest of the shower. These images were recorded by the new camera of the CT5 H.E.S.S. telescope, NamCAM. Credit: H.E.S.S. Collaboration.

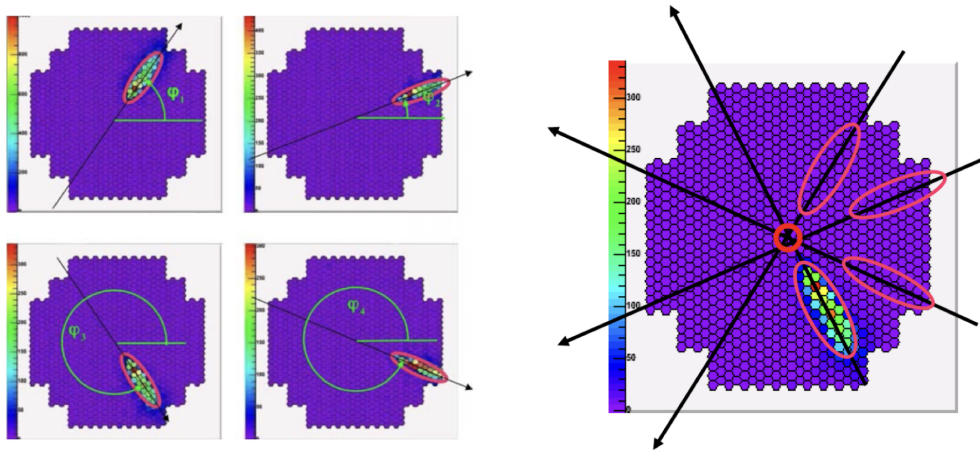


Figure 30: Left: shower images in four small cameras of H.E.S.S. Right: the four images are combined in the same virtual camera plane. The intersection of image axes gives the position of the source in the sky. Credit: H.E.S.S. Collaboration.

The captured images can also be utilized to reconstruct the *shower core*, which is the name given to the position where the primary particle trajectory intersects with the ground. This is achieved by analyzing the angles φ shown on the left plots of Figure 30. On the contrary to the source position reconstruction, this time the positions of the telescopes are retained, and the ϕ angle values are combined to determine the position of the core (Figure 31). This figure also illustrates the fact that combining the core position and the direction of the incoming shower allows to increase the precision of shower direction reconstruction.

Pointing From what we have seen in the previous paragraphs, it appears it is crucial to maintain accurate pointing and camera positioning in the focal plane to ensure reliable results. Of course, this is true in general, and not only in the case of the Hillas analysis.

To check pointing capabilities of each H.E.S.S. telescope, and to correct any inaccuracy, the telescopes are pointed at a particular star with a known position, obtained from a catalog. The lid of the Cherenkov camera is closed, and it is used as a screen on which the star's image is focused. Then, a picture of the star's image on the camera lid is taken with a CCD camera located on the main

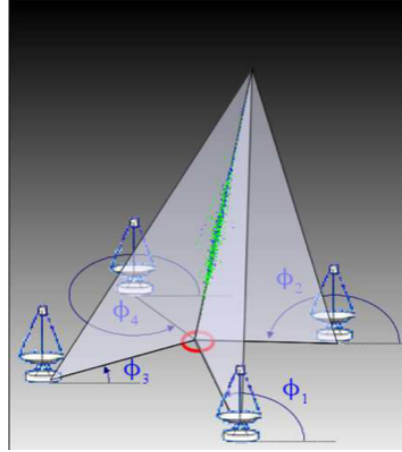


Figure 31: The shower core is reconstructed from the azimuthal angles measured by each telescope. Note that the situation depicted in Figure 30 (left) is not the same as the one shown here. Figure from [3].

mirror support structure. In addition, on the camera lid, eight LEDs (Light Emitting Diodes) are turned on. The image of the star is typically centred on the lid plane. The position of the star is used to check pointing accuracy: the (RA, DEC) coordinates of the star from the catalog should match the coordinates at which the telescopes have been pointed at. On the other hand, the LEDs are used to detect the exact position of the camera with respect to the telescope mechanical structure. In particular, it is used to correct for any tilt angle (rotation around the optical axis), which would result in a decrease of performance.

Gamma-hadron separation In addition to the reconstruction of the position of the source and of the shower core, Hillas parameters are also used for gamma-hadron¹⁴ separation. Various techniques have been developed, including the *Scaled Cuts* method we are going to discuss here. As we know, the elliptical shape of the gamma-ray-induced shower images is in contrast to the irregular shape of hadron-induced images. The nature (gamma-like or hadron-like) of the incoming particle can then be assessed from the results of the fit of the ellipse. This is done by comparing the image parameters (length L and width W) with the expected values and variance of the same variables obtained from simulations with different charges q (in p.e.) and impact distances ρ , the distance between the shower core and the telescope position.

Scaled Width (SW) and Scaled Length (SL) are defined by:

$$SW = \frac{w(q, \rho) - \langle w(q, \rho) \rangle}{\sigma_w(q, \rho)}, \text{ and } SL = \frac{l(q, \rho) - \langle l(q, \rho) \rangle}{\sigma_l(q, \rho)}. \quad (8)$$

For stereoscopic observations with $ntels$ telescopes, we obtain the *Mean Scaled Width* (MSW) and the *Mean Scaled Length* (MSL):

$$MSW = \frac{\sum_{tels} SW}{\sqrt{ntels}}, \text{ and } MSL = \frac{\sum_{tels} SL}{\sqrt{ntels}}. \quad (9)$$

¹⁴Actually, rather than “gamma-hadron” separation, we should use “gamma-like vs hadron-like” separation instead. Remembering §2.3, the discrimination procedure will only allow us to separate between gamma-like and hadron-like events.

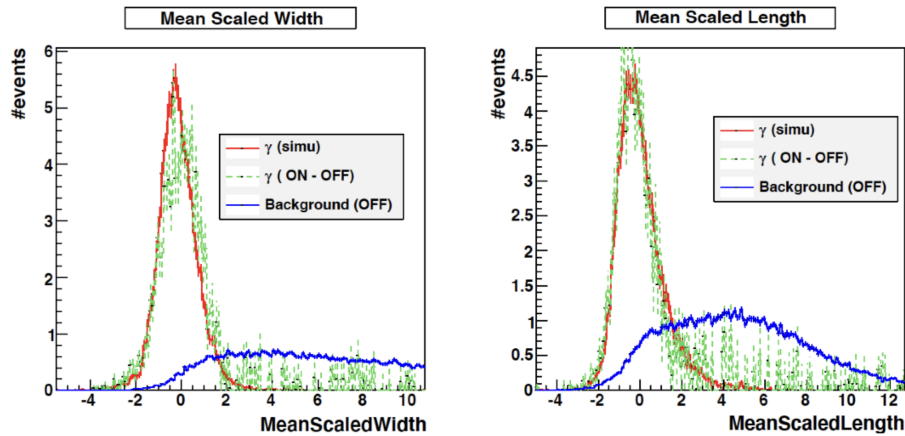


Figure 32: An example of *MSW* (left) and *MSL* (right) distributions for a dataset obtained observing the Crab Nebula. Simulated gamma-rays are shown in red, real reconstructed gamma-like events are shown in green, and real background events are in blue. The meaning of “ON”, “OFF”, and “ON-OFF” will be explained later in §5.2. from [3].

Figure 32 shows an example of *MSW* and *MSL* distributions for observations of the Crab Nebula.

From this figure, it is interesting to point out that photons are located on the left of the distribution (small values of *MSW* and *MSL*), while the hadrons give a broader peak which is shifted on the right. This difference allows for the selection of gamma-like events using a particular cut, e.g. $MSW < 1$. In this particular case, most of the background will be rejected, but still, some hadrons will remain. This is an illustration of the fact the discrimination procedure only produces a list of gamma-like events, and that there may still be a small hadronic contamination. The lower the cut will be (e.g. $MSW < -1$), the higher the purity of the selected sample will be. However, this will significantly reduce the statistics.

One of the primary advantages of using Scaled Cuts is that they are scaled by the variance of the parameters, meaning that the energies of the events do not influence the selection efficiency. At small energies, showers have greater fluctuations (bigger variance), resulting in smaller scaled parameters while at higher energies, showers are more similar to each other (smaller variance), which leads to larger parameters. As a result, there is no bias in the energy spectrum determination.

Energy reconstruction The two key ingredients for energy reconstruction are the intensity also referred to as the “size” of the image, corresponding to the total number of photo-electrons collected, and the distance of the shower core. The higher the energy, the higher the number of p.e., the higher the size. In addition, for a given energy, if the shower falls at a greater distance, the intensity will be reduced. Several methods can be used to reconstruct the energy. Some use random forest algorithms [22], and some use Look-Up Tables (LUTs). Here we will give a short description of the use of LUTs.

To generate the LUTs, a large amount of data is simulated and organized into tables that cover a large range of impact distances and sizes. For each simulated shower, the impact point (or core) is reconstructed, and the image size (intensity) in each telescope is computed. The events are

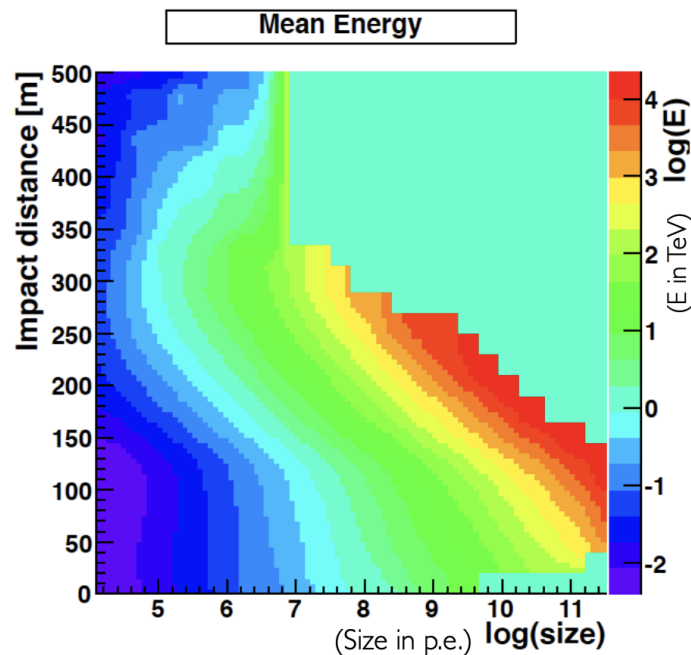


Figure 33: An example of a LUT, as represented by a 3D histogram. Figure from [3].

then binned based on the reconstructed distance to the telescope and image intensity. For each bin, the average and variance of the true energy (known, since we are working with Monte Carlo simulations) are computed.

Several tables are generated to account for different observational conditions, with different values of zenith angles, optical efficiencies, and offset angles. Interpolation is used to generate intermediate values as necessary. An example of LUT, as seen as a 3D histogram, is shown in Figure 33. The true energy is shown as a color scale (note the logarithmic scale) as a function of size in p.e. (X axis, logarithmic scale) and impact distance (Y axis).

The process of reconstructing the true energy of the primary particle begins with obtaining the image parameters, followed by the determination of the shower size and impact distance. Next, a LUT is used to obtain the corresponding true energy for each telescope. For a telescope array, the final energy estimation is obtained from a weighted average of the values given by all telescopes.

The accuracy of the energy estimation is indicated by the energy resolution. For the method described here, it is typically around $\sim 20\%$, with small biases observed at low and high energies.

5.1.2 Model reconstruction

Another reconstruction method is used by the H.E.S.S. collaboration, known as “*Model reconstruction*”, which was developed by De Naurois and Rolland [6] based on an earlier work by Le Bohec et al. [23] in the late 1990s. This approach typically allows a sensitivity improvement by a factor of two compared to Hillas reconstruction. Improvement of a factor two in sensitivity would be equivalent to multiply the number of telescopes by four.

Basic principle The basic principle of the Model reconstruction is to compare calibrated images obtained from real data with calibrated images obtained from simulated showers of known

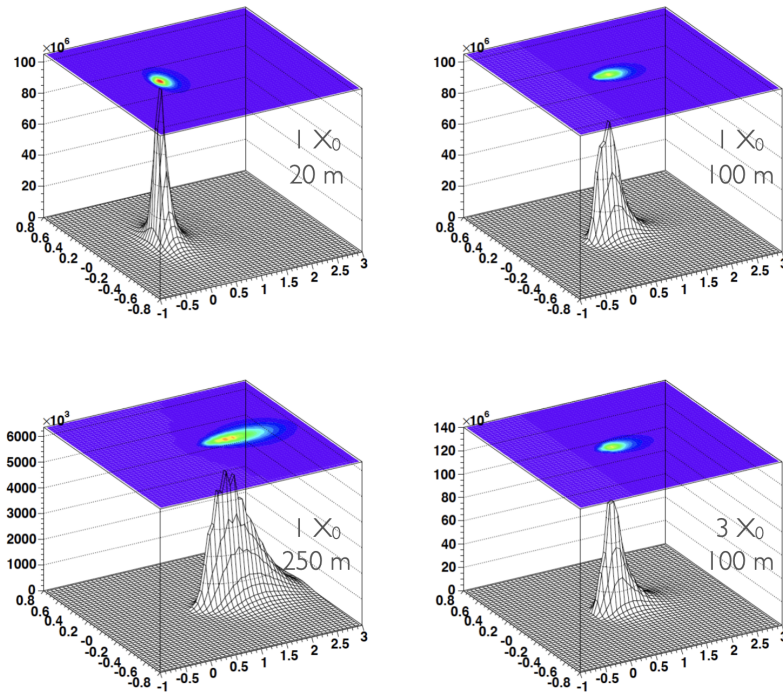


Figure 34: Examples of modelled shower images for 1 TeV vertical showers at different impact distances: 20 m (top left), 250 m (bottom left), and 100 m (right column). Also, two values for the first interaction depth are shown: $3 X_0$ for the bottom right plot (the shower starts deeper in the atmosphere), and $1 X_0$ for all the other images. X,Y units: degrees in the camera frame; Z scale: intensity in p.e. Pixel size is 0.01 deg. Figure from [3].

characteristics. Because this technique requires a large number of simulated showers, using a fully detailed description of the physics of cascades for each data set would be extremely time consuming. Instead, Monte Carlo simulations are used only to build a semi-analytical model. The Cherenkov emission of a shower is entirely deduced from the longitudinal, lateral and angular distributions of the charged particles. These distributions are produced from Monte Carlo simulations, and parameterized to build models of showers, where the first interaction depth is also taken into account. Once the model is set, it is used to generate the shower images as obtained by the cameras (raw data). The NSB contribution is also taken into account. The calibration software is then used to produce calibrated data. Reconstruction and gamma-hadron separation are achieved using a log-likelihood maximization technique, identifying the best match between the modeled calibrated images and the images obtained from data.

Building and validating the model The main ingredient of the method is the model used to parameterize the showers. Figure 34 shows some examples of modelled shower images for a 1 TeV vertical gamma-induced showers, and for different input parameters: distance of the shower core, and depth of the first interaction. Note that this depth is expressed in radiation length units ($X_0 \approx 36.7 \text{ g.cm}^{-2}$ for the atmosphere). These images show the output of simulations in the camera frame, and without NSB.

Once the model has been built, it is essential to verify its accuracy by comparing it with full

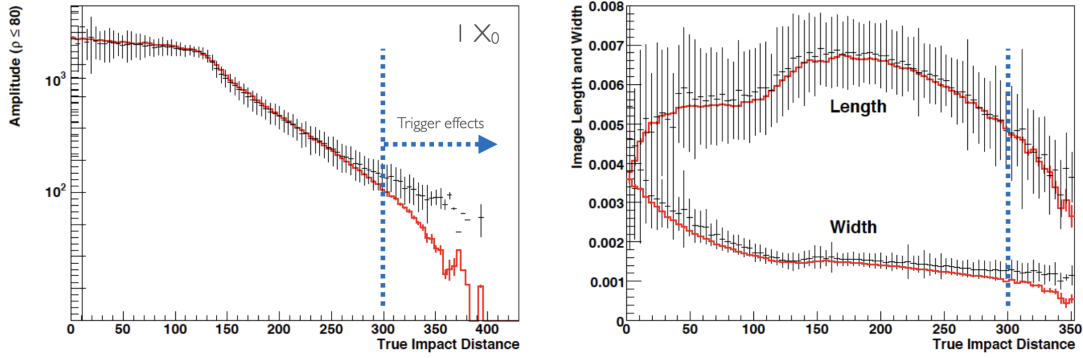


Figure 35: Comparison between the model and the simulations. Average and shower-to-shower fluctuations from simulations are shown in black (1 TeV, zenith). Model prediction is shown in red. Left: amplitude (size) of the image as a function of the impact distance. Right: length and width as a function of impact distance. In both plots, the model is very accurate up to an impact distance of ~ 300 m. Above that limits, the discrepancies can be interpreted as coming from trigger effects. Figure from [3].

simulations of the showers. An example of such a comparison is shown in Figure 35 where the model prediction is shown as a red curve while black points are obtained from the simulated shower images. For the distribution of the impact distance with a first interaction depth at one radiation length (Figure 35, left), the model works well, except for large impact distances (> 300 m). The same assessment can also be made looking at image width and length (Figure 35, right).

The discrepancy is due to trigger effects. Namely, when the shower core is far from the camera, the total size is less than ~ 100 p.e., this charge being spread over many pixels. Statistical fluctuations can cause similar showers to be just above the trigger threshold and others to be just below it. When showers fluctuate to higher intensities, they are more likely to trigger the camera, leading to a higher average image amplitude in the simulation as compared to the model. Shower to shower fluctuations, shown as error bars on the plots, cannot be taken into account in the model.

Shower parameter reconstruction A comparison is made between real camera images and millions of modelled showers images, including NSB. To accomplish this, a likelihood fit is performed, which compares the real images (the charge in p.e. in each pixel; pixels are assumed to be independent) with the model. This comparison aims at reconstructing energy, direction (two parameters), impact location (two parameters), and first interaction depth, so a total of six parameters.

These six parameters come with associated uncertainties, the covariance matrix and the final log-likelihood value, which is used to assess the goodness of the fit parameter defined by:

$$G = \frac{\sum_{\text{pixel } i} [\ln L(s_i | \mu_i) - \langle \ln L \rangle_{\mu_i}]}{\sqrt{2 \times \text{NDoF}}}, \quad (10)$$

where:

- $L(s_i | \mu_i)$ is the pixel log-likelihood, with s the signal and μ the expectation value;
- $\sqrt{2 \times \text{NDoF}}$ is the normalisation, here with $\text{NDoF} = \text{number of pixels} - 6$.

Parameter G behaves asymptotically like a χ^2 function and thus provides an evaluation of the fit quality.

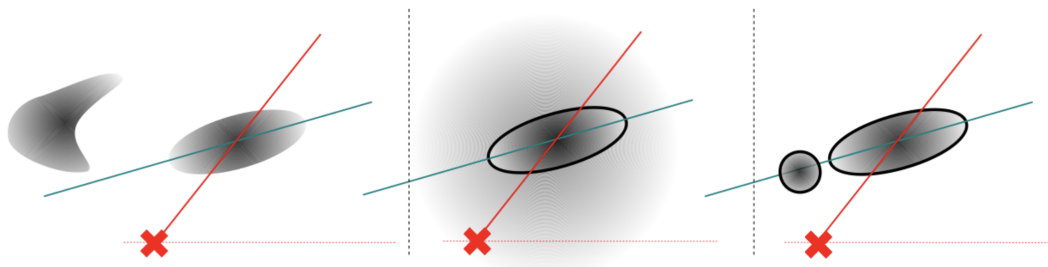


Figure 36: Discrimination between gamma-ray and hadron-induced showers relies on several facts: Left: hadron-induced showers are irregular, and the image usually shows clusters. Middle: hadronic part of the shower produces low-intensity Cherenkov light which is spread over the camera (“hadronic rain”). Right: primary charged particle can produce direct Cherenkov light. On the three plots, the red cross corresponds to the center of the camera. Figure from [6].

Gamma-hadron separation From the obtained parameters, it is possible to discriminate between gamma-like events and hadron-like events by considering certain features of the hadronic showers. First, hadronic showers can show clusters (Figure 36, left). Second, the hadronic part of the shower produces Cherenkov light due to the charged particles motion, which result in a blurred area around the main emission, referred to as “hadronic rain” (Figure 36, middle). Finally, the primary charged particle can emit direct Cherenkov light, which appears as a small cluster in addition to the bulk of the hadronic shower (Figure 36, right).

From these facts, discriminant variables are designed, called *ShowerGoodness* (SG) and *BackgroundGoodness* (BG). The variable SG is built in a similar way as the goodness-of-fit G , but with pixels identified as being part of the shower image: all pixels with a charge > 0.01 p.e. are considered, together with three rows of neighbours. The variable BG is built in a same way, but considering all remaining pixels, where clusters and hadronic rain will contribute.

Figure 37 shows the distributions of the variable SG for a data set obtained by H.E.S.S. observing the blazar PKS 2155-304. The red histogram is obtained from a pure gamma-ray sample produced by Monte Carlo simulations, taking into account a NSB contribution of 40 MHz p.e. The blue histogram corresponds to the measured signal (excess events) and the grey one to background events.

As for the Hillas reconstruction (see Eq. 9), we can define a new parameter called *Mean Scaled Shower Goodness* ($MSSG$) to be used for stereoscopic observations:

$$MSSG = \frac{\sum_{\text{tels}} SG}{\sqrt{ntels}}, \quad (11)$$

where $ntels$ is the number of telescopes.

5.1.3 From reconstruction to analysis, and detector performance

We now have seen how to reconstruct the shower parameters from calibrated data, either by using the Hillas, or the Model method. Both provide the primary particle parameters, as well as a way to discriminate between gamma-like and hadron-like events.

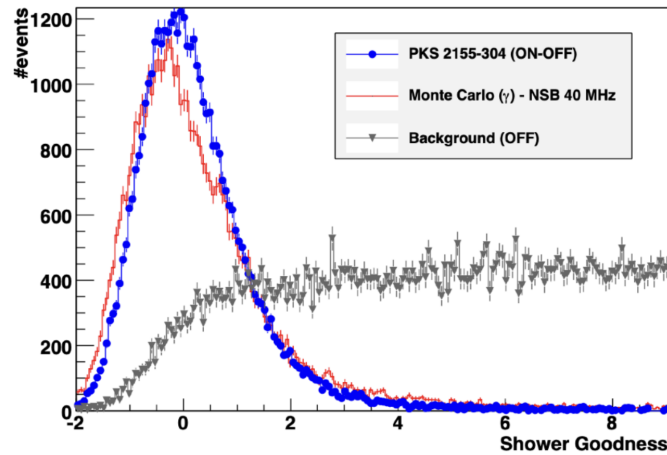


Figure 37: Distribution of the *ShowerGoodness* discrimination variable obtained with a H.E.S.S. dataset for the blazar PKS 2155-304. The red histogram is obtained from a pure gamma-ray sample produced by Monte Carlo simulations. The blue histogram corresponds to the measured signal (excess events) and the grey one to background events. The meaning of “ON”, “OFF”, and “ON-OFF” will be explained later in §5.2. Figure from [6].

Selection cuts Before we run the reconstruction, a series of initial selections are made. Focusing on the Model reconstruction, these selections are applied on the following parameters:

- The minimum charge (in p.e.) in the camera. Events with a very small number of photoelectrons in the camera may not provide enough information for accurate parameter reconstruction.
- The maximum nominal distance (degrees) between the shower image centroid and the center of the camera. Showers that fall too far from the telescopes are removed since they usually give only a small amount of Cherenkov light.
- The minimum number of telescopes required. It can be decided that at least two telescopes are necessary so that stereoscopy can be used.
- The maximum *ShowerGoodness* (see the example given in Figure 37), which will be the main discrimination criteria to select only gamma-like events.
- The range for primary depth (X_0 units).

Here, it is extremely important to stress that different sets of selection cuts will lead to different performance. For example, some cuts will give better performance at low energies, while other will be optimized for high energies. Also, each set of cuts will give different lists of reconstructed events. The same event could be reconstructed as gamma-like with a particular set of cuts, and as hadron-like with other cuts. It is therefore very important to choose the cuts with great care, depending on which type of objects are observed.

After reconstruction, another selection cut is made on the parameter θ^2 , where θ is the angle between the expected position of the source and its reconstructed position. For a point-like source,

events coming from a direction which is far from the direction of the source are most likely background events.

In H.E.S.S., standard sets of cuts are available (Table 1). These sets are applied depending on the characteristics of the source being studied. Loose (less stringent) cuts may be used to retain more events for statistical purposes but at the cost of a higher contamination by hadronic-like events. In general, the faint source cuts are applied to sources with a low flux and a hard spectrum¹⁵. In that case, it is possible to use a smaller cut on θ^2 . On the other hand, loose cuts are used for sources with a high flux and a soft spectrum¹⁶.

Name	Min. Charge (p.e.)	Max. Nom. Distance (deg.)	#Tels	SG_{\max}	t_0 (X_0)	θ_{\max}^2 (deg ²)
Standard	60	2	2	0.6	[-1, 4]	0.01
Faint Source	120	2	2	0.4	[-1, 4]	0.005
Loose Cuts	40	2	2	0.9	N/A	0.0125

Table 1: Standard cuts used in H.E.S.S. for the Model reconstruction.

Performance The efficiency of the reconstruction process is evaluated based on the following criteria:

- Its ability to recover shower parameters with accuracy.
- Its ability to reject hadron background.

The detector's performance is typically quantified using specific parameters such as the *effective area*, and the *migration matrix*. The effective area has the dimension of a surface area, and gives a quantitative indication on detection and reconstruction efficiency. When convoluted with a flux (photons per unit of surface and time), the effective area allows to obtain the number of detected photons per unit of time. The migration matrix allows to recover the relation between the true energy (E_{true}), and reconstructed energy (E_{rec}). By construction, it also contains information on energy resolution (the spread of the reconstructed energy) and bias (the difference between the true energy and the average reconstructed energy). These parameters collectively contribute to the so-called *Instrument Response Functions* (IRFs).

Public datasets provided by some collaborations (such as *Fermi*) are distributed together with a set of IRFs obtained for different configurations of the reconstruction procedure. It is up to the user to ensure that he or she uses the correct set of IRFs for the analysis he or she intend to perform.

The detector's performance is contingent on various observational conditions and so are IRFs. They depend on zenith angle, offset angle, type of reconstruction, cleaning thresholds (for the Hillas method), and selection cuts used for reconstruction.

Figure 38 shows the effective area of the H.E.S.S. array for different reconstruction settings (Hillas and Model, with various sets of cuts), for a source at zenith. It can clearly be seen that the Model reconstruction with loose cuts (see Table 1) results in a higher effective area at low energies,

¹⁵For equal integrated fluxes, a hard spectrum has a higher flux at high energies than a soft spectrum.

¹⁶See the previous footnote.

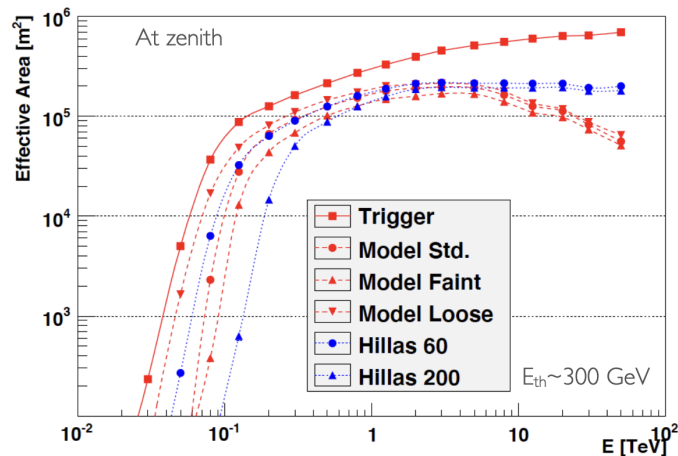


Figure 38: Effective area as a function of the energy for different reconstruction methods and settings, for a source at zenith. The curve labeled “Trigger” is above all the others. It corresponds to the showers which trigger the array, whatever their type. “Hillas 60” and “Hillas 200” correspond to Hillas reconstruction, with two different minimum charge settings: 60 p.e. and 200 p.e. Figure from [3].

here below ~ 1 TeV. We can also notice that Hillas reconstruction give better performance above ~ 2 TeV.

Focusing on the performance at low energies, it is worth mentioning here a very important parameter of gamma-ray experiments: the *energy threshold*. We can have a rough idea of the threshold by looking at which energy the effective area increases sharply, here slightly above ~ 300 GeV. However, the energy threshold is defined in a more rigorous way: it is the maximum of the convolution between a power law spectrum (usually taken with a power index of -2) and the effective area. As a result of this definition, it is entirely possible to observe events reconstructed with energies lower than the threshold...

Figure 39 shows the energy resolution and bias (inset) for three reconstruction settings. Here again, it can clearly be noticed that the resolution and bias depend on the type of reconstruction method implemented, as well as on the cuts applied.

Another crucial component of the IRFs is the *migration matrix*. An example is depicted in Figure 40 as a 2D histogram. The migration matrix gives the relation between the true energy (X axis) and the reconstructed energy (Y axis). In such a plot, the energy bias becomes notably apparent, here at low energies (blue rectangle). This discrepancy can be attributed to trigger efficiency, which decrease at low energies, leading to an overestimation of the reconstructed energy.

5.1.4 Summary

After the calibration step, reconstruction allows to identify incoming particles as gamma-like or hadron-like using discriminating variables. In addition, it provides the energy, the direction of the incoming particle, the location of the core¹⁷.

As we have seen, numerous factors require consideration in the context of the reconstruction process. It is important to remember that at the end, it is impossible to eliminate the occurrence of

¹⁷Remember, the core is the location where the primary particle would hit the ground.

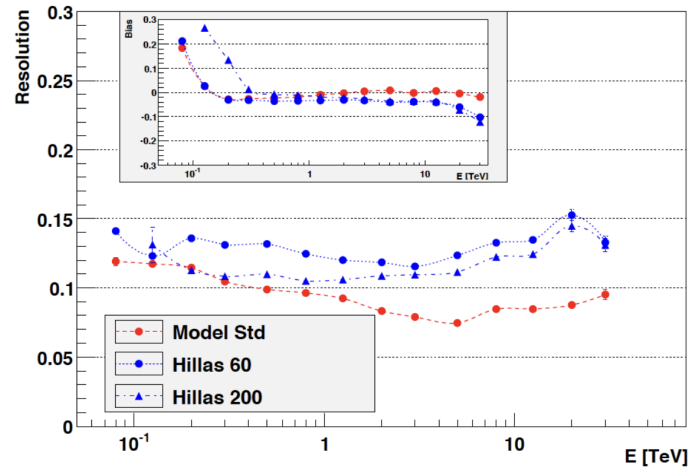


Figure 39: Energy resolution as a function of the energy for different reconstruction methods and settings. Figure from [3].

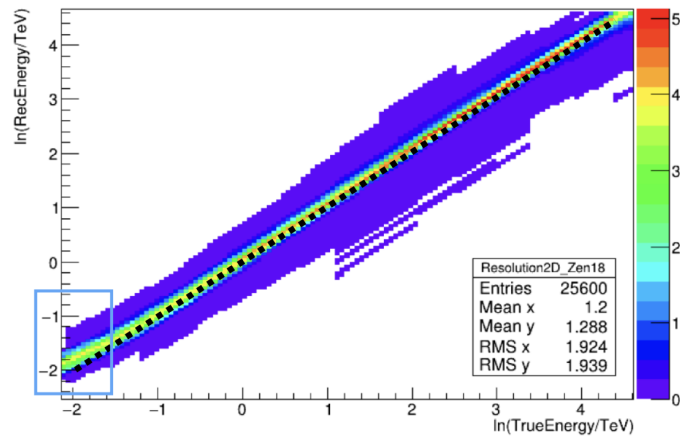


Figure 40: The migration matrix depicted as a 2D histogram. Note that both scales are logarithmic. See the text for further details. Credit: H.E.S.S. Collaboration.

hadrons in the gamma-like sample. This is illustrated in Figure 41 where a typical distribution for a discrimination variable is shown for pure gamma-ray sample (gray histogram) and a pure proton sample. The gamma-like events include:

- Real gamma from the source under study.
- Real gamma from the gamma-ray backgrounds, galactic and extragalactic.
- Real electrons. Electrons also give electromagnetic showers. It is then difficult to separate them from photons.
- Real hadrons misidentified as photons.

Real gamma from the source under study are the photons we want to isolate further, enabling the extraction of source properties such as spectrum, light curve, and morphology. To achieve this,

it is essential to estimate the background with the utmost accuracy. This will be the goal of the next step, analysis.

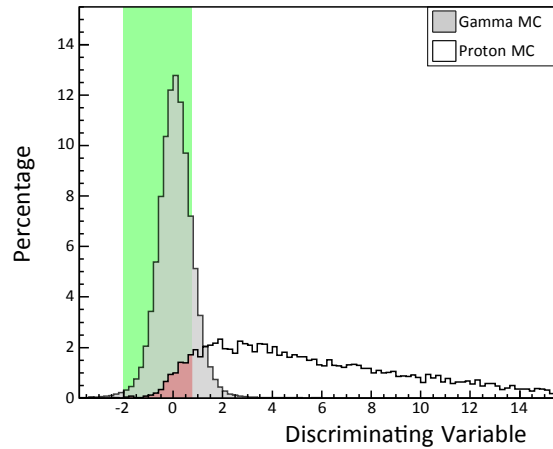


Figure 41: Gamma events are selected by performing a cut (green area) on a discrimination variable. As can be seen, a small fraction of real hadrons are included (dark red area), hence the name “gamma-like”. Figure from [3].

5.2 Analysis

The successful detection of a cosmic source generally necessitates multiple observation runs, which can be conducted over a long period of time, and which are typically taken under various conditions, with different zenith angles, offset angles, etc. Also, some runs may be affected by potential hardware-related issues. The primary objective of the analysis is to combine these individual runs to yield an accurate estimate of the background.

5.2.1 Background estimation

Some background estimation techniques require the knowledge of the detector’s *acceptance*, defined as the probability that a certain type of event of a given energy will trigger the system, be reconstructed, and be selected according to a pre-established event class. Such techniques involve extensive use of simulations. This is not the case for a technique such as the one called “Multiple-OFF”, which we will discuss in the following.

The background is estimated from the effective field of view (FoV) of the array (Figure 42). The telescopes of the array are pointed to the observation position, with an offset angle with the position of the source under study. A so-called “*ON region*” is defined around the position of the source, where the signal is expected to be. It can happen that other sources are also present in the FoV. In that case, it is important to remove them so that they do not contribute to the background estimation. For that purpose, “*exclusion regions*” are defined (dark blue areas in Figure 43). Note that the ON region is also an exclusion region since it cannot be used to estimate the background. The “*OFF regions*” are defined so that they have the same size as the ON region, they do not overlap with any exclusion region, and they are laid out at the same distance from the observed position than the ON region (green circle). This pattern ensures the detection efficiency is the same for all

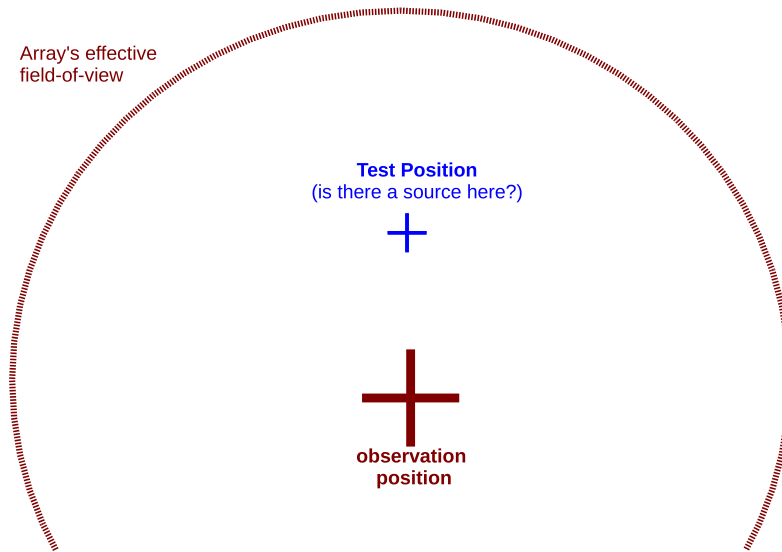


Figure 42: The field of view of the array is centered on the large red cross corresponding to the observed position in the sky. The test position of the source under study (blue cross) is shifted by the “*offset angle*”. Courtesy of K. Kosack.

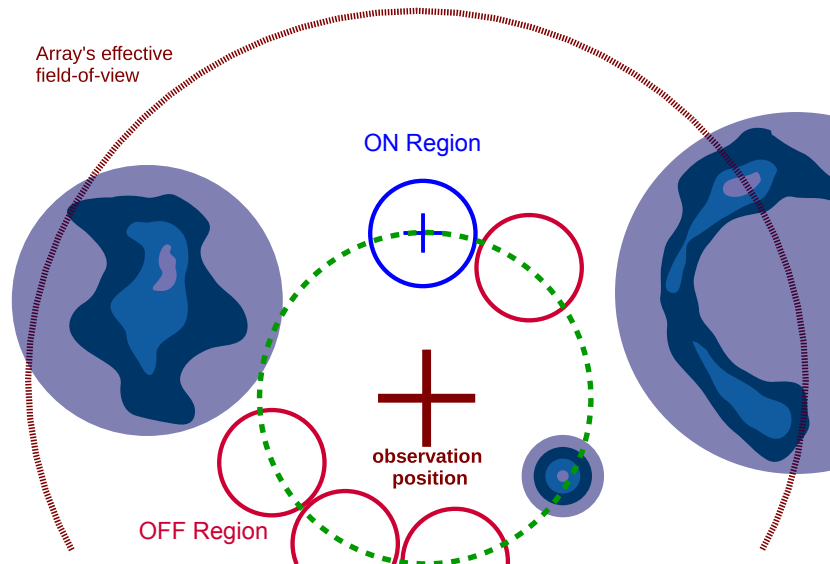


Figure 43: The blue circles corresponds to the ON region, which is the area of interest. The dark blue areas are exclusion regions. The red circles highlight the four OFF regions which can be used for background estimation. Note that the OFF regions are chosen so that they are symmetric around the observation position. Courtesy of K. Kosack.

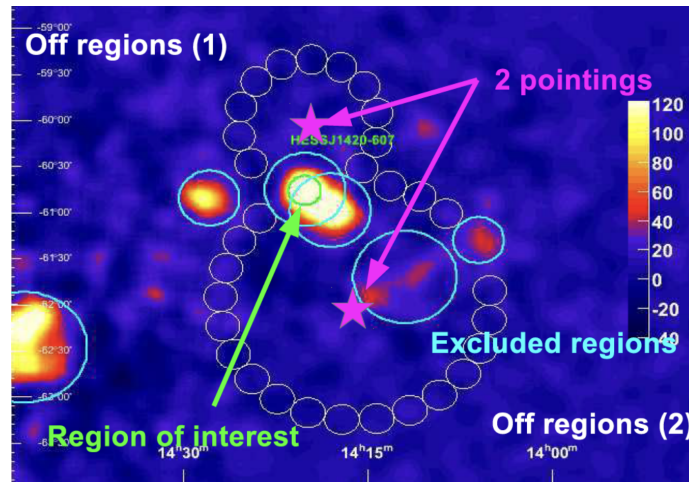


Figure 44: An example of an observation by H.E.S.S., featuring the region of interest outlined in green, with an adjacent cyan exclusion zone. Additional exclusion zones account for acknowledged sources within the FoV. Small grey circles indicate the OFF regions, which are defined in two distinct sets due to variations in pointing configurations. Figure from [3].

OFF regions as well as for the ON region. There are often several OFF regions, hence the name “Multiple OFF”.

Figure 44 shows a real example of an observation carried out by the H.E.S.S. array, where two different pointing positions were used. The region of interest is shown by a green circle and surrounded by an exclusion zone (light blue). Several other exclusion regions are defined to account for known sources within the FoV. The small grey circles represent the OFF regions, with two distinct sets corresponding to the two pointing positions.

In some cases, tens of data-taking runs are necessary to comprehensively study a specific source. It can sometimes be a tedious process to define all excluded regions, but it has to be done with great care nonetheless. A badly defined exclusion region could lead to biases in the final results. Control plots (see Figure 45 below as an example) are used to control these possible biases and eliminate them.

5.2.2 Significance

Statistical significance is used to confirm the detection of a source. Namely, it is used to assess if the signal dominates over the background and to what extent. The convention for confirming the detection of a source typically necessitates that the statistical significance exceeds a threshold of five standard deviations (5σ).

The significance is defined from three parameters:

- N_{on} , the number of events in the region of interest (ROI, the ON region).
- N_{off} , the number of events in control regions (OFF regions).
- α , the ratio of the expected number of background events in the ROI over the actual number of background events accumulated in OFF regions. α can be understood as the ratio of exposures between the ON region and the OFF regions.

From these variables, the *excess* is defined by $N_{\text{on}} - \alpha N_{\text{off}}$, and the corresponding significance is given [24] by

$$S = \sqrt{-2 \ln \lambda}, \quad (12)$$

with:

$$\lambda = \left[\frac{\alpha}{1 + \alpha} \left(\frac{N_{\text{on}} + N_{\text{off}}}{N_{\text{on}}} \right) \right]^{N_{\text{on}}} \times \left[\frac{1}{1 + \alpha} \left(\frac{N_{\text{on}} + N_{\text{off}}}{N_{\text{off}}} \right) \right]^{N_{\text{off}}}. \quad (13)$$

In this last expression, λ is actually the likelihood-ratio between two hypotheses. The first hypothesis is that the N_{on} events result from both signal events (expectation value S , not to be mixed up with the significance S) and background events (expectation value αB): $N_{\text{on}} = S + \alpha B$. The second one is that N_{on} result only from background events (αB). It corresponds to the *null hypothesis*.

5.2.3 Control plots

At least two types of plots are usually used to check that both reconstruction and analysis are sound. The first one is the distribution of significance S (given by Equation 12, not to be confused with the expectation value S), as shown in Figure 45 (left). On such a plot, the pure background events show up as a Gaussian distribution with zero average and standard deviation equal to one (red curve). The excess events, those which are identified as true gamma-rays coming from the source appear as a tail in the distribution.

Another important plot to look at is the θ^2 distribution¹⁸ (Figure 45, right, and Figure 46). These plots show two different situations. On Figure 45 (right), the background contribution is negligible. The parameters displayed on the plot confirm that, with $N_{\text{on}} = 10621$, and $N_{\text{off}} = 753$. While we can read on the plot “ $\alpha = 11.97$ ”, the value¹⁹ given is actually $1/\alpha$ (see the previous paragraph), meaning that $\alpha = 0.083$. Using this value with the numbers given for N_{on} and N_{off} , we can retrieve the value of the excess: $N_{\text{on}} - \alpha N_{\text{off}} = 10558$. The signal to background ratio is given by:

$$S/B = \frac{N_{\text{on}} - \alpha N_{\text{off}}}{\alpha N_{\text{off}}}, \quad (14)$$

which gives $S/B = 167.8$. The significance is 221σ , and the flux of gamma-rays is evaluated to be 134 min^{-1} . The *live time* is also given on the plot. It corresponds to the observation time, corrected²⁰ by the dead-time (see §3.3.2).

Figure 46 gives another example with a higher level of background. It is now possible to see the distribution of θ^2 for the OFF regions. In that particular case, the angle θ is measured with respect to the center of the OFF region. As expected for the background, this distribution is flat. A slope in this histogram would indicate a problem, e.g. the presence of a gamma-ray source in one of the OFF regions.

On both Figure 45, right, and Figure 46, the cuts on θ^2 are shown. On Figure 46, it is apparent how this cut is used to improve the S/B ratio.

¹⁸Remember that θ is the angular distance between the position of the source in the camera and the position where it is expected to be.

¹⁹It is a matter of convention. The H.E.S.S. collaboration decided to define its α as $1/\alpha'$, where α' is the parameter α of these lecture notes. We did not want to confuse the reader by adding a new notation just to use it on two plots.

²⁰If the observation is one hour long, and if the dead-time is such that the camera accept new events only 50% of the time, the live time is 30 minutes.

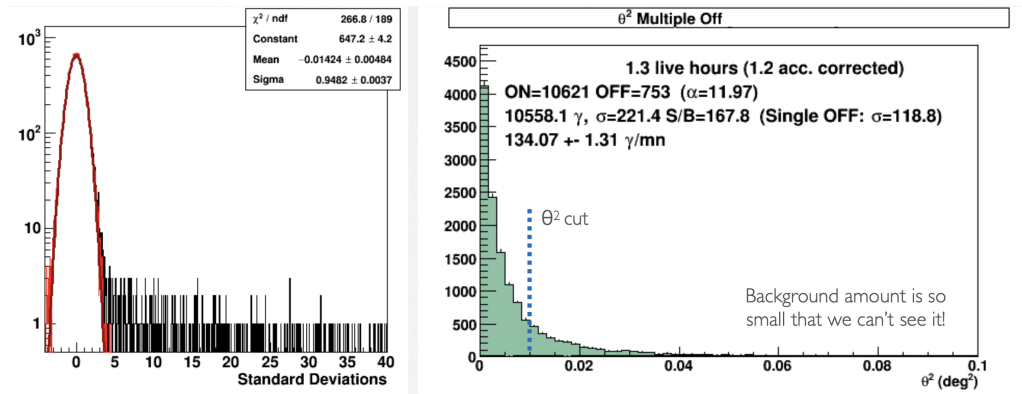


Figure 45: Two control plots used to check the analysis results. Left: distribution of significance. Right: θ^2 distribution. Although the background contribution is shown on the plot, it is too low to be visible. See the text for more details. Credit: H.E.S.S. Collaboration.

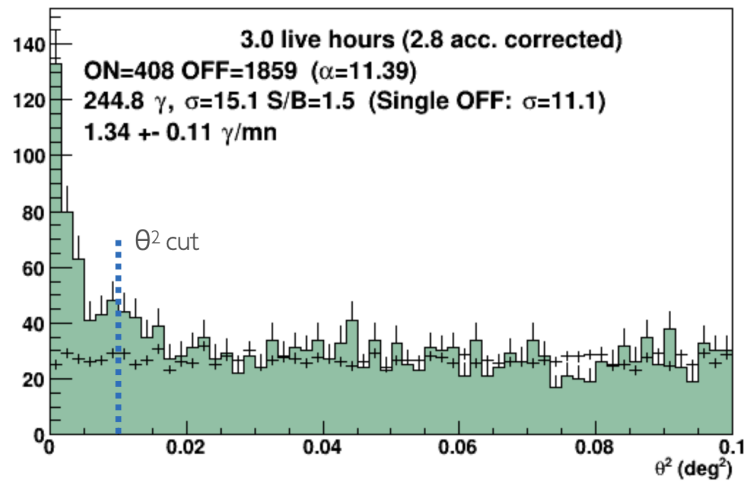


Figure 46: Another example of a θ^2 plot for a source with a visible background contribution. The θ^2 distribution for the ON region is depicted in green, while the plus signs show the distribution for the OFF regions. The ON distribution decreases towards the value obtained for the OFF regions. Credit: H.E.S.S. Collaboration.

5.2.4 A glimpse on spectrum determination

Before a Lorentz Invariance Violation (LIV) analysis can be attempted, the energy spectrum and the light curve of the source need to be obtained. The spectrum is simply the energy distribution and the light curve is the flux as a function of time.

The techniques in use to extract the spectrum and the light curve are quite complex, and since these lecture notes are already quite long, we will only give a quick overview on how the spectrum is obtained using the so-called “*forward folding*” method [25].

The forward folding method requires a thorough understanding of the instrument, that is detailed knowledge of the IRFs: migration matrix (true energy E_{true} vs reconstructed energy E_{rec}), energy resolution (\mathcal{R}), effective area (\mathcal{A}). It is important to emphasise again that IRFs vary depending on

reconstruction type, selection cuts and specific observation conditions.

First, a function Φ is assumed to represent the spectrum shape, from a set of parameters $\vec{\alpha}$. It can be either a power law, or a broken power law, a log-parabola, a log-parabola with an exponential cutoff, or another type of function. Second, using the assumed spectral shape, the expected number n_γ of gamma events for each energy bin $[E_{rec,1}, E_{rec,2}]$ is computed:

$$n_\gamma = \int_{E_{rec,1}}^{E_{rec,2}} dE_{rec} \int_0^\infty dE_{true} \mathcal{R}(E_{rec}, E_{true} | \delta, \Psi, \epsilon) \times \mathcal{A}(E_{true} | \delta, \Psi, \epsilon) \times \Phi(E_{true} | \vec{\alpha}), \quad (15)$$

where δ is the zenith angle, Ψ the off-axis angle and ϵ the optical efficiency. At the next step, a log-likelihood method is used to compare the expected number of gamma events in each energy bin against the number of detected events. The corresponding probability density function is obtained from the number of ON and OFF events, taking into account the live-time normalisation, $\beta = T_{on}/T_{off}$:

$$P(N_{on}, N_{off} | n_\gamma, n_h) = \frac{n_\gamma + \beta n_h^{N_{on}}}{N_{on}!} e^{-(n_\gamma + \beta n_h)} \times \frac{n_h^{N_{off}}}{N_{off}!} e^{-n_h}, \quad (16)$$

where n_γ and n_h are the expected numbers of gamma and background events in the energy bin.

The results of the likelihood maximisation process include:

- best fit parameters, $\vec{\alpha}_{best}$,
- the expected number of events in each energy bin,
- the covariance matrix, which is used to derive the flux uncertainty in each bin,
- the final value of the log-likelihood which is used as a goodness-of-fit parameter.

Figure 47 shows an example of a spectrum obtained with the forward folding method. Interestingly, the points shown are not calculated directly from the data. Instead, each point is derived from the model using the best-fit parameters and the residuals in each energy bin. The fitted function is then drawn, and the points are obtained from the residuals.

The reconstruction of the light curve in a given energy bin is quite similar to the forward folding technique, except that both time and energy bins have to be considered in the likelihood fit. Once the energy range is chosen, the flux is evaluated within each individual time bin.

Before we move to the last section of these lecture notes, it is necessary to discuss a very important notion that each reader should know: sensitivity.

5.2.5 Sensitivity

It can be interesting to have a way to compare the performance of the detector with the ones of other instruments, whether they are of the same type or not. For this, we commonly use the *sensitivity*, which is the minimum flux that can be detected with a given level of significance and for a given observation duration. Once the settings for reconstruction and analysis have been decided, sensitivity is assessed using Monte Carlo simulations.

Figure 48 on page 56 shows a sensitivity plot comparing the future performance of CTA with the ones of several other experiments. In this case, the sensitivity is derived for a 5σ significance and 50-hours of observations, for a point-like source. Under the conditions shown, the southern array can detect a flux as low as 10^{-13} erg cm⁻² s⁻¹ at the 5σ level in 50 hours.

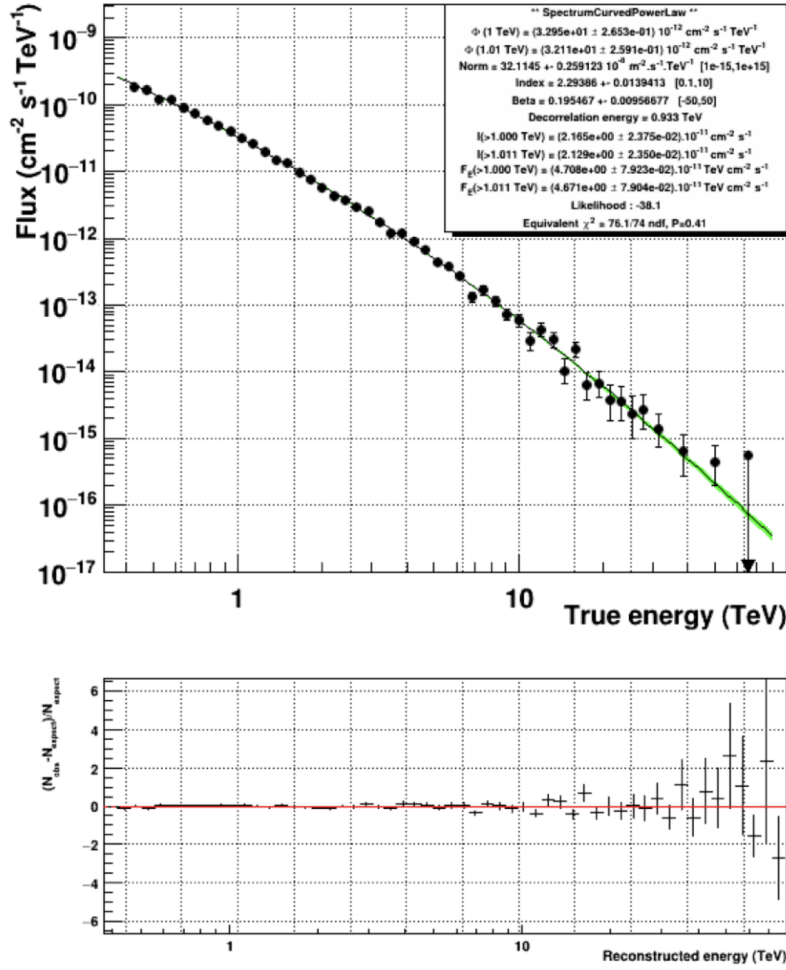


Figure 47: Example of a spectrum obtained with the forward folding method. The reconstructed model is represented in green. The points are obtained from the residuals shown in the bottom panel. Credit: H.E.S.S. Collaboration.

6. Lorentz invariance violation analysis

In this section, we will only give a short insight into the Lorentz Invariance Violation (LIV) analysis, focusing on the search for energy-dependent time delays, and on the related requirements for hardware and analysis. For the details, we refer the reader to the lecture notes in these series by Elisa Prandini et al. [26] and A. Campoy-Ordaz et al. (lecture notes of the COST Action CA18108 third training school, to be published). We also refer the reader to section 5.1.3 of the COST Action CA18108 review [27].

To test for LIV using imaging atmospheric Cherenkov telescopes (IACTs), we start from a model-independent photon dispersion relation in vacuum, modified with energy-dependent terms:

$$E^2 = p^2 c^2 \times \left[1 + \sum_{n=1}^{\infty} S_n \left(\frac{E}{E_{QG,n}} \right)^n \right], \quad (17)$$

where E and p are respectively the energy and momentum of a VHE gamma ray, c is the Lorentz

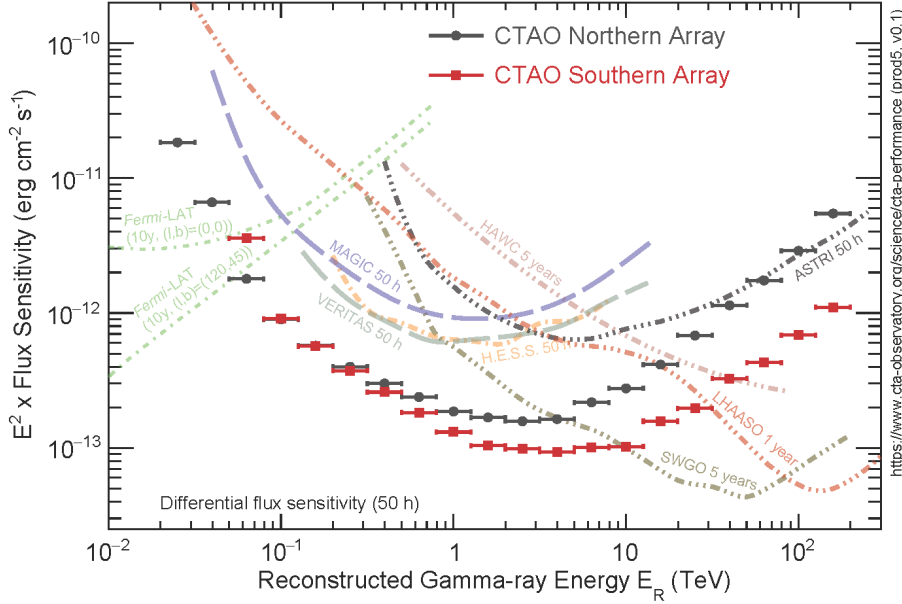


Figure 48: Differential sensitivities for the CTA northern and southern arrays for 50 hours of observation. The sensitivity curves are compared with the ones of other experiments. Plot taken from <https://www.cta-observatory.org/science/cta-performance/>.

invariant speed of light, and $E_{QG,n}$ is the energy scale at which effects of quantum gravity are supposed to become significant²¹. Only the first two leading terms ($n = 1$ or $n = 2$) of the series expansion have been tested so far. The energy-dependent photon group velocity can be derived from the previous equation. If $S_n = +1$, the result is a velocity greater than c (superluminal motion). If, on the other hand $S_n = -1$, the velocity is less than c (subluminal motion). If one assumes energy-dependent propagation velocities, two photons of different energies ($E_2 > E_1$) emitted simultaneously from a distant source (redshift z_s) have different, energy-dependent times of arrival (t_1 and t_2). The energy-dependent time delay is given by:

$$\Delta t = t_2 - t_1 \simeq -S_n \frac{n+1}{2} \frac{E_2^n - E_1^n}{E_{QG,n}^n} D_n(z_s), \quad (18)$$

where parameter $D_n(z_s)$ is the distance contribution which takes into account the Universe expansion. For the most straightforward phenomenological approaches which have been considered so far, this term increases with distance, as we could expect (see e.g. [28]).

From Equation 18, we first notice that the redshift (or distance) of the source has to be known. For a GRB, for example, for which the flux decrease with time, this implies that the Cherenkov telescopes need to be fast enough to point to the source as soon as possible. This criteria has a profound impact on the mechanical design. Besides, time and energy of each event needs to be measured with the highest accuracy. Time precision is directly related to the hardware in use, for example GPS receivers. For the energy, the reconstruction and analysis processes are very

²¹ E_{QG} should be related in some way to the Planck scale $E_P \sim 10^{19}$ GeV.

important: cuts must be chosen, algorithms must be tweaked in such a way the energy resolution is the best possible, and the energy bias is the smallest possible. Also, the rejection factor needs to be as high as possible so that the photon sample is as pure as possible.

As of now, no significant time delay was measured, and limits were set on E_{QG} . When deriving the limits, statistical and systematic uncertainties must be evaluated with great care. Some of the systematic uncertainties rely on the specific method used to measure the time lag, but the others are related to selection cuts, energy resolution, energy calibration, etc. In the effort to get more constraining limits on Quantum Gravity energy scale, it is then essential to put a significant effort on reconstruction and analysis.

7. Conclusion

The aim of these lecture notes is to provide a comprehensive introduction to data collection, reconstruction and analysis in ground-based gamma-ray astronomy. As the reader noticed, the topic is huge and require a good understanding on various topics, some of them even related to hardware. It is often the case, indeed, that a good understanding of the data requires a good understanding on how a detector work. Of course, some points have been deliberately ignored in these notes because we think they are of lesser interest for a reader discovering the topic, either experimentalist or theorist. The references given below will help the interested reader to discover more on the technicalities we ignored.

Some experiments already provide their data to the whole community. This will be more and more the case for all major present and future experiments and observatories (such as CTA). We hope the readers will have a good view on what are ground-based gamma-ray data, how they are collected, calibrated, reconstructed, and analyzed. Most importantly, we hope these notes will prevent the readers from falling into a couple of gaping traps: considering reconstruction or analysis software as a black box, and taking public data for granted.

Acknowledgements

The authors thank the anonymous reviewer for their careful review of this manuscript. JB is very grateful to JS and ACO, who prepared the first version of the draft. JS acknowledges funding from the University of Rijeka, project number uniri-prirod-18-48. ACO is gratefully acknowledged by the financial support of the Spanish grant PID2019-107847RB-C42, funded by MCIN/AEI/ 10.13039/501100011033. JB warmly thanks his colleagues from H.E.S.S. and CTA who kindly provided some of the plots reproduced in these notes, in particular M. De Naurois, K. Kosack, J.-P. Lenain, S. Ohm, and F. Toussenel. Finally, the authors would like to acknowledge networking support by the COST Action CA18108.

References

- [1] F.A. Aharonian and C.W. Akerlof, *Gamma-Ray Astronomy with Imaging Atmospheric Cherenkov Telescopes*, *Annual Review of Nuclear and Particle Science* **47** (1997) 273.
- [2] M. de Naurois, *L'expérience CELESTE: Reconversion d'une centrale solaire pour l'astronomie gamma. Première observation de la Nébuleuse du Crabe et du Blazar Markarian 421 entre 30 et 300 GeV*, PhD Theses, Université Pierre et Marie Curie - Paris VI, May, 2000.
- [3] M. de Naurois, *Very High Energy astronomy from H.E.S.S. to CTA. Opening of a new astronomical window on the non-thermal Universe*, habilitation à diriger des recherches, Université Pierre et Marie Curie - Paris VI, Mar., 2012.
- [4] J.E. Ward, J. Cortina and D. Guberman, *Light-Trap: a SiPM upgrade for VHE astronomy and beyond*, *Journal of Instrumentation* **11** (2016) C11007 [[1710.07807](#)].
- [5] A.M. Hillas, *Cherenkov Light Images of EAS Produced by Primary Gamma Rays and by Nuclei*, in *19th International Cosmic Ray Conference (ICRC19)*, Volume 3, vol. 3 of *International Cosmic Ray Conference*, p. 445, Aug., 1985.
- [6] M. de Naurois and L. Rolland, *A high performance likelihood reconstruction of γ -rays for imaging atmospheric Cherenkov telescopes*, *Astroparticle Physics* **32** (2009) 231 [[0907.2610](#)].
- [7] F. Aharonian, A. Akhperjanian, K.-M. Aye, A. Bazer-Bachi, M. Beilicke, W. Benbow et al., *Calibration of cameras of the H.E.S.S. detector*, *Astroparticle Physics* **22** (2004) 109.
- [8] J. Aleksić, S. Ansoldi, L. Antonelli, P. Antoranz, A. Babic, P. Bangale et al., *The major upgrade of the MAGIC telescopes, part i: The hardware improvements and the commissioning of the system*, *Astroparticle Physics* **72** (2016) 61.
- [9] G. Pühlhofer, C. Bauer, A. Biland, D. Florin, C. Föhr, A. Gadola et al., *FlashCam: A fully digital camera for CTA telescopes*, in *AIP Conference Proceedings*, AIP, 2012, [DOI](#).

- [10] J. Bolmont, P. Corona, P. Gauron, P. Ghislain, C. Goffin, L. Guevara Riveros et al., *The camera of the fifth H.E.S.S. telescope. Part I: System description*, *Nuclear Instruments and Methods in Physics Research A* **761** (2014) 46 [1310.5877].
- [11] M. Punch, *Winston Cones for Light-Collection and Albedo Protection in CAT*, in *International Workshop Towards a Major Atmospheric Cerenkov Detector-III for TeV Astro/Particle Physics*, 5, 1994.
- [12] C. Perennes, M. Doro, D. Corti, L. Lessio, M. Mallamaci, M. Mariotti et al., *Optical feasibility of an upgrade of the CTA LST camera to SiPM*, *Nucl. Instrum. Meth. A* **984** (2020) 164485.
- [13] S. Billotta, D. Marano, G. Bonanno, M. Belluso, A. Grillo, S. Garozzo et al., *SiPM Detectors for the ASTRI project in the framework of the Cherenkov Telescope Array*, in *Proc. SPIE Astronomical Telescopes + Instrumentation*, vol. 9154 of *High Energy, Optical, and Infrared Detectors for Astronomy VI*, 2014, DOI.
- [14] Hamamatsu Photonics K.K. Editorial Committee, *Photomultiplier Tubes, Basics and Applications, 4th Edition*, Hamamatsu Photonics K.K. Electron Tube Division (2017).
- [15] T. Ashton, M. Backes, A. Balzer, D. Berge, J. Bolmont, S. Bonnefoy et al., *A nectar-based upgrade for the cherenkov cameras of the H.E.S.S. 12-meter telescopes*, *Astroparticle Physics* **118** (2020) 102425.
- [16] R. Chalmé-Calvet, *Étalonnage du cinquième télescope de l'expérience H.E.S.S. et observation du Centre Galactique au delà de 30 GeV*, theses, Université Pierre et Marie Curie - Paris VI, Nov., 2015.
- [17] M. Tsirou, *Study of Pulsar Wind Nebulae in Very-High-Energy gamma-rays with H.E.S.S.*, theses, Université Montpellier, Oct., 2019.
- [18] C. Fruck and M. Gaug, *Atmospheric monitoring in MAGIC and data corrections*, in *European Physical Journal Web of Conferences*, vol. 89 of *European Physical Journal Web of Conferences*, p. 02003, Mar., 2015, DOI.
- [19] A. Charbonnier, *De la recherche de matière noire à l'émission diffuse de rayons gamma dans l'expérience H.E.S.S.*, theses, Université Pierre et Marie Curie - Paris VI, Nov., 2010.
- [20] T.C. Weekes, M.F. Cawley, D.J. Fegan, K.G. Gibbs, A.M. Hillas, P.W. Kowk et al., *Observation of TeV Gamma Rays from the Crab Nebula Using the Atmospheric Cerenkov Imaging Technique*, *ApJ* **342** (1989) 379.
- [21] S. De, W. Maitra, V. Rentala and A.M. Thalpillil, *Deep learning techniques for imaging air Cherenkov telescopes*, *Phys. Rev. D* **107** (2023) 083026 [2206.05296].
- [22] K. Ishio and D. Paneque, *A novel energy reconstruction method for the MAGIC stereoscopic observation*, *arXiv e-prints* (2022) arXiv:2212.03592 [2212.03592].

- [23] S. Le Bohec, B. Degrange, M. Punch, A. Barrau, R. Bazer-Bachi, H. Cabot et al., *A new analysis method for very high definition imaging atmospheric Cherenkov telescopes as applied to the CAT telescope.*, *Nuclear Instruments and Methods in Physics Research A* **416** (1998) 425 [[astro-ph/9804133](#)].
- [24] T.P. Li and Y.Q. Ma, *Analysis methods for results in gamma-ray astronomy.*, *ApJ* **272** (1983) 317.
- [25] F. Piron, A. Djannati-Atai, M. Punch, J.P. Tavernet, A. Barrau, R. Bazer-Bachi et al., *Temporal and spectral gamma-ray properties of Mkn 421 above 250 GeV from CAT observations between 1996 and 2000*, *A&A* **374** (2001) 895 [[astro-ph/0106196](#)].
- [26] E. Prandini, K. Dialektopoulos and J. Strišković, *Gamma rays: propagation and detection*, *PoS CORFU2021* (2022) 319.
- [27] A. Addazi, J. Alvarez-Muniz, R. Alves Batista, G. Amelino-Camelia, V. Antonelli, M. Arzano et al., *Quantum gravity phenomenology at the dawn of the multi-messenger era – A review*, *Progress in Particle and Nuclear Physics* **125** (2022) 103948 [[2111.05659](#)].
- [28] U. Jacob and T. Piran, *Lorentz-violation-induced arrival delays of cosmological particles*, *Journal of Cosmology and Astroparticle Physics* **2008** (2008) 031.